

Chapter 4

Charge transfer in amorphous systems

Although it is important to know the maximum bound on the mobility of the charge carrier in a perfect crystal of an organic semiconductor, in reality it is very difficult to control defect formation in OSs^{76?}. This is due to van der Waals forces only weakly holding molecules at lattice sites, allowing molecules greater freedom than in traditional inorganic crystal, and increasing the chance of defect formation which can trap/scatter charge carriers reducing overall mobility. This means it is important to investigate and characterise charge transport properties for not just perfectly crystalline OSs but also those that show a range of amorphicity.

In this chapter I investigate how structural disorder of the OS, on top of thermal disorder, changes the physical nature of the charge carrier, its localization length, transport mechanism and mobility. In particular, the degree of structural disorder at which the flickering polaron loses its delocalized character and becomes localized. This is important because a decrease in charge carrier delocalization correlates with a decrease in charge mobility, the essential result of transient localisation theory. To do so, I present quantum dynamical calculations of the charge carrier dynamics at room temperature in a number of samples of pentacene with varying levels of crystallinity, from fully amorphous to perfectly crystalline. The quantum dynamical simulation method, denoted fragment orbital-based surface hopping (FOB-SH), is well suited for this task because it makes no assumptions with regard to the charge transport mechanism. FOB-SH was shown to predict charge mobilities well over several orders of magnitude but it has so far only been

applied to single crystalline OS. Methodological developments by me and other members of the Blumberger group have now made it possible to apply this novel methodology, for the first time, to large samples of disordered OS with different nanoscale morphologies.

The molecule chosen to investigate amorphous films was pentacene. This molecule is a popular organic semiconductor and the subject of much research due to its high field effect mobility⁷⁷, use in device applications⁷⁸ and, more recently, the use of functionalization to alter device properties^{79,80}. The pentacene molecule consists of 5 joined benzene rings (36 atoms) and crystals typically pack with a herringbone motif as shown in figure 4.1.

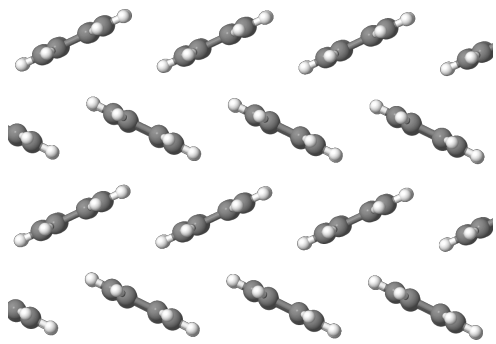


Figure 4.1: An example of the herringbone packing typically found in Pentacene crystals

4.1 Creating Amorphous Pentacene

In order to create the amorphous pentacene systems a melt-quench technique was used. This is a standard technique, often used to create amorphous systems in both computational and experimental fields^{81–85}. The procedure followed is shown in figure 4.2.

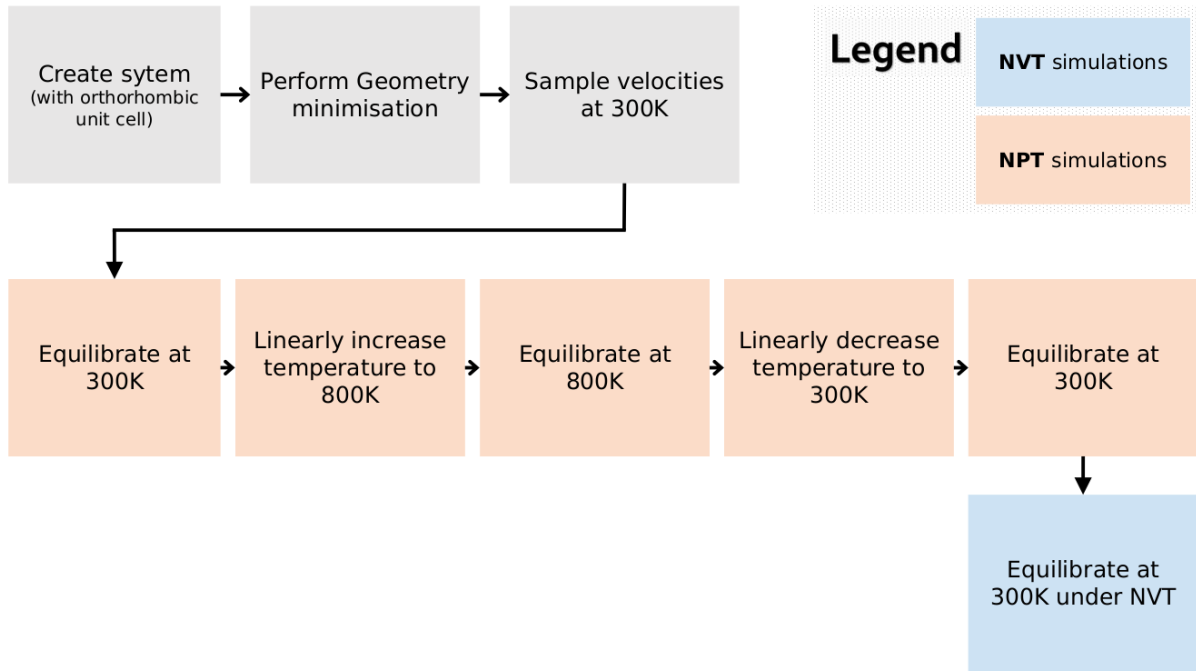


Figure 4.2: The melt-quench scheme used to create amorphous pentacene systems. Blue boxes indicate steps using an NPT ensemble, orange boxes indicate use of a NVT ensemble.

In this procedure, the system was initialised with an individual pentacene molecule on a regular 3D grid using an orthorhombic unit cell. This was chosen to make analysis of the resulting structures easier than with the triclinic unit cell typically used to simulate pentacene crystals. The velocities were initially randomly sampled from a gaussian distribution and a Nose-Hoover thermostat and barostat was used to control the temperature and pressure. The Lammps molecular dynamics package was used^{86,87} and electrostatic interactions were handled with Lammps' particle-particle-particle-mesh ewald method⁸⁸. RESP⁸⁹ (restrained electrostatic potential) partial charges were parameterised using Gaussian 16⁹⁰ with the B3-LYP level of theory and a 6-311g(d) basis set. The use of partial charges was essential in the creation of the amorphous systems and neglecting them lead to unphysical face-to-face stacking of pentacene molecules. This is shown in figure 4.10, in section 4.3.1. Finally, for inter and intra molecular interactions the general

AMBER force-field⁹¹ (GAFF) was applied. There isn't one predominant forcefield used in simulations of pentacene in the literature, though parameters from GAFF have been used and validated in a number of studies^{92–98}.

Four different quenching times were used spanning 4 orders of magnitude: 0ns, 1ns, 10ns and 100ns. For the 0ns, 1ns and 10ns quenching simulations 3,000 molecules were simulated. In the 100ns quenched structure 3060 molecules were simulated. The initial structure for the 1ns and 10ns quenched structures were taken from a restart of the 0ns quenched simulation after the 800K equilibration step. The 0ns and 1ns quenched structure were carried out under 1 atmosphere of pressure in x, y and z. However, the 10ns quenching required a small increase to 5 atmospheres as the structure had a tendency to deform such that one of the cell vectors became either very large or very small. In the 100ns quenched structure I updated the barostat target pressure (before the phase transition) to account for similar deviations in simulation box dimensions.

4.2 Structure of the quenched simulations

A movie showing the full 100ns melt-quench simulation can be found here: <https://youtu.be/6IQ-cYErQHVs>. Still images of the final snapshot of each different quenching time are shown in figure 4.3.

4.2.1 Final Structure Snapshots

We can see qualitatively that as we increase the quenching time from a) → d) the structure starts to look more ordered and crystal layers are starting to be formed. Looking longer at the structure we see that lower quench times tend to form small crystal clusters. In the 0ns quenched structure these clusters tend to be just ~7-10 molecules in size. As we increase the quenching time to 1ns we see 1D channels of crystalline pentacene start to form throughout the structure, though the structure is still relatively disordered due to these channels being randomly oriented with respect to one another. As we increase the quenching time these crystal fragments become larger until in the 100ns quenched structure the whole system is comprised of just 2 crystals. The reason for this is, as the rate of cooling is decreased, the rate of crystal seeding is also decreased. That is, at longer

quenching times, more time is spent in states where it is only just energetically favourable for a crystal to be seeded. When a crystal is seeded it can grow very quickly through the system, as the crystal packing is normally the lowest energy packing state. At longer quench times, the initial crystal fragment can propagate through the system before any other crystals have the chance to form, hence creating large single crystals in the system. At shorter quench times, we pass very quickly into a temperature that makes it very easy for crystals to be seeded. This results in many areas of the system starting to crystallise at once and these crystals then impede the further propagation of their neighbours. This can be seen in the animation of the [100ns melt quench simulation](#) linked above.

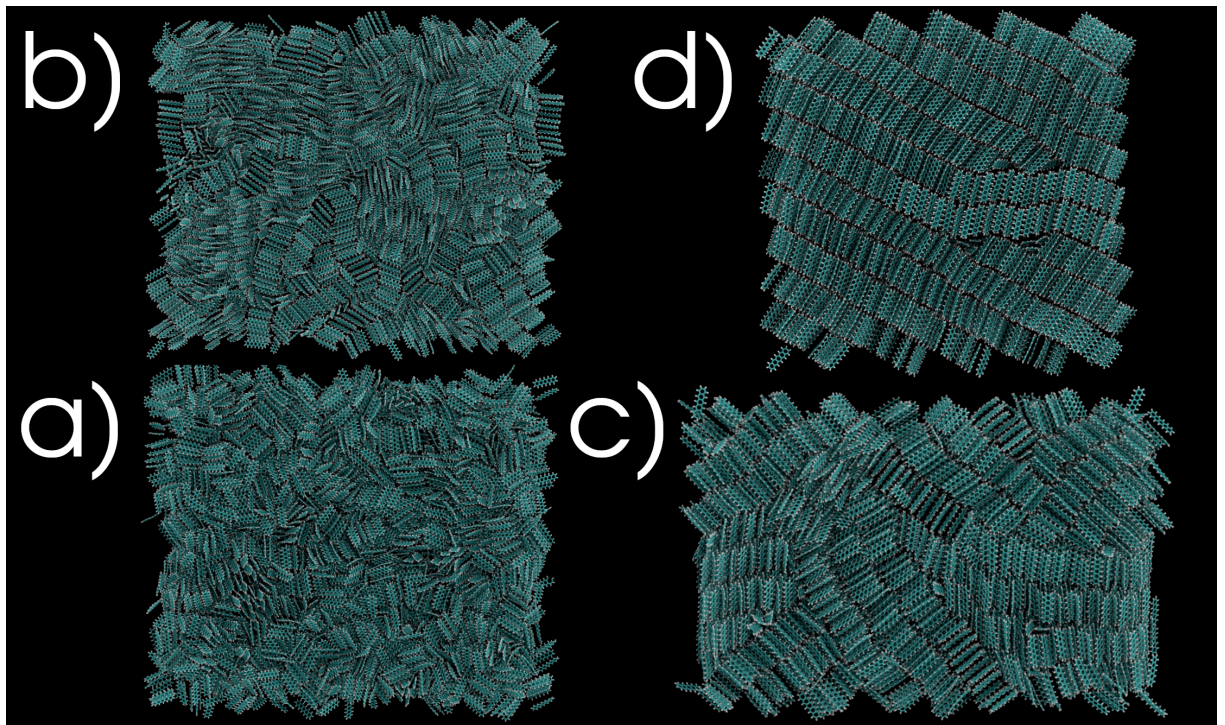


Figure 4.3: The final snapshot of each quenching simulation visualised in VMD⁴ and rendered with Tachyon⁵. Snapshots are ordered by quenching time i.e. a) is the 0ns quench, b) is the 1ns quench and so on.

4.2.2 Molecular Packing

We can isolate clusters in each of the different structures shown in figure 4.3 to reveal the molecular packing within. In figure 4.4 a DBSCAN-like algorithm has been applied to the final structure from the 100ns quench to cluster molecules based on the molecular density in a given region of space. These clusters have then been high-

lighted by different colours. The top-most green cluster has been rotated such that, on the left, we are viewing it at an angle perpendicular to the plane of molecules, as shown by the cartoon eye. Comparing this plane to the crystal plane to the right, we can see a striking similarity in the packing motif. The herringbone packing has formed and (as can be seen in figure 4.7 in section 4.2.4) the herringbone intersection angle is remarkably similar to the crystal plane. This serves as a confirmation of the choice of force-field and the parameterisation of the partial charges.

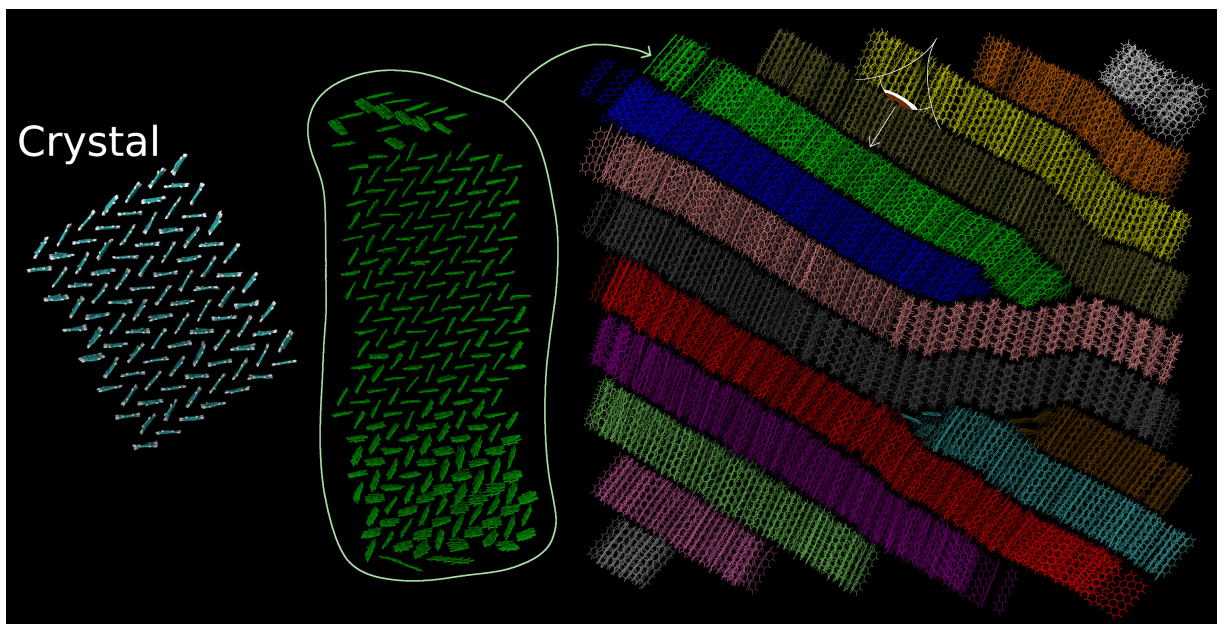


Figure 4.4: The 100ns quenched structure with different clusters shown with different colours. A bird's eye view of the green cluster has been shown on the left to demonstrate the herringbone packing within each cluster/layer. The far-right image labelled 'Crystal' is a snapshot of a crystal plane after a short MD equilibration.

Although this herringbone packing pattern is most obvious in the 100ns quenched structure, it can also be seen in the other structures. At the other extreme in the 0ns quenched structure we see small clusters (<10 mol) of pentacene crystals forming. This is shown in figure 4.5. At this quenching time (0-50 ps) it was energetically favourable for many regions of the structure to start to crystallise at once. This

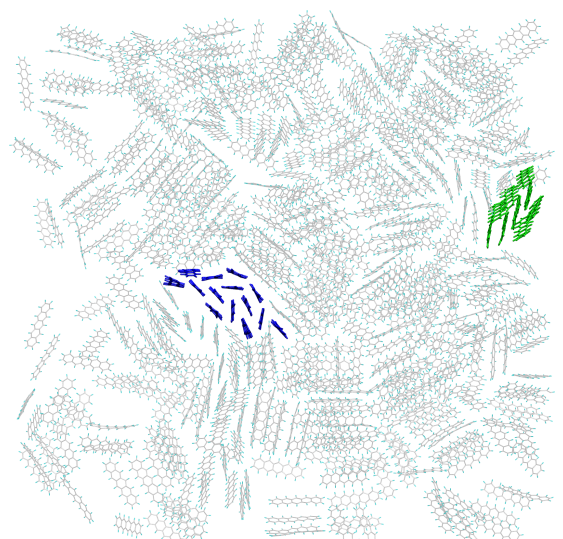


Figure 4.5: A slice from the 0ns quenched structure with 2 selected clusters displaying herringbone-like packing.

resulted in a high density of crystal fragments growing into each other and stopping when a neighbouring crystal fragment was encountered. In figure 4.5, 2 such clusters are shown in blue and green. In both clusters the packing motif has become very herringbone-like. However, due to their small size they are more affected by the surrounding environment which warps the structure slightly.

To quantify the change in the structure for the differently quenched structures 3 macroscopic properties have been plotted: the mass density, the angular distribution and the radial distribution function. These are discussed in the following sections.

4.2.3 Mass Density

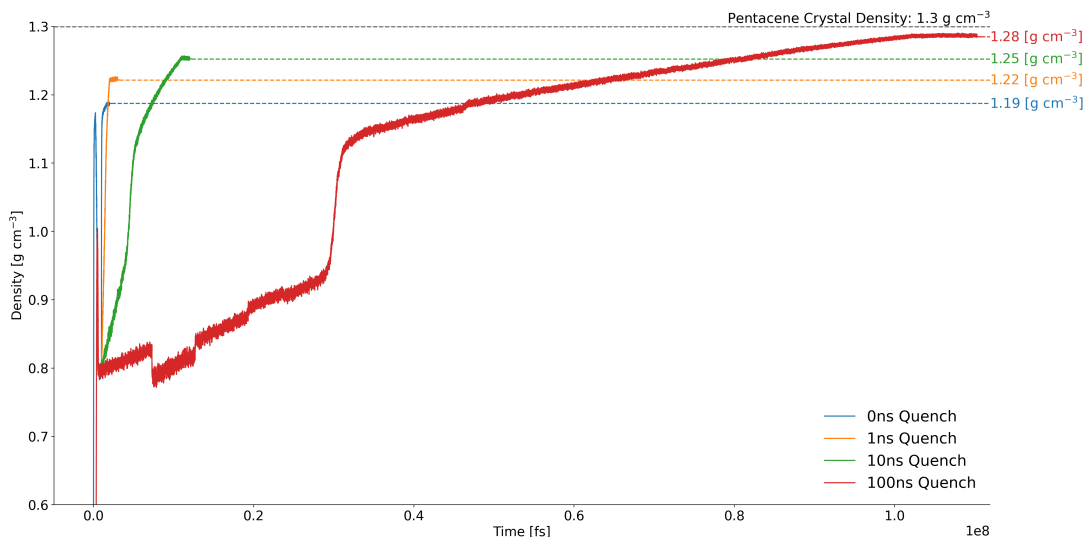


Figure 4.6: A time series of the density of the quenched structures. The black line shows the experimental mass density of crystal pentacene.

The mass density of the 4 different quenching simulations can be seen in figure 4.6. This was calculated by dividing the total mass of the atoms in the system by the volume (product of cell vectors) of the simulation box. The first thing to notice in this graph is as we increase the quenching time we increase the density of the final sample. This is due to the molecules packing more efficiently in the crystal than in an amorphous structure. We also see very clearly in the plots the sudden increase in density associated with the phase transition from liquid to solid Pentacene. In the 1ns quench structure (quenched with the barostat set to 1 atmosphere) this occurs around Pentacene's experimental melting

of 530.15K⁹⁹ providing confirmation of the choice of force-field. The 0ns, 1ns and 10ns runs were performed in a single 24 hour run. The 100ns quench was performed using many restarts, the discontinuities in the density for the 100ns structure come from these restarts. These do not affect the final structure as these only occur while the system is in the liquid state.

4.2.4 Angular Distribution

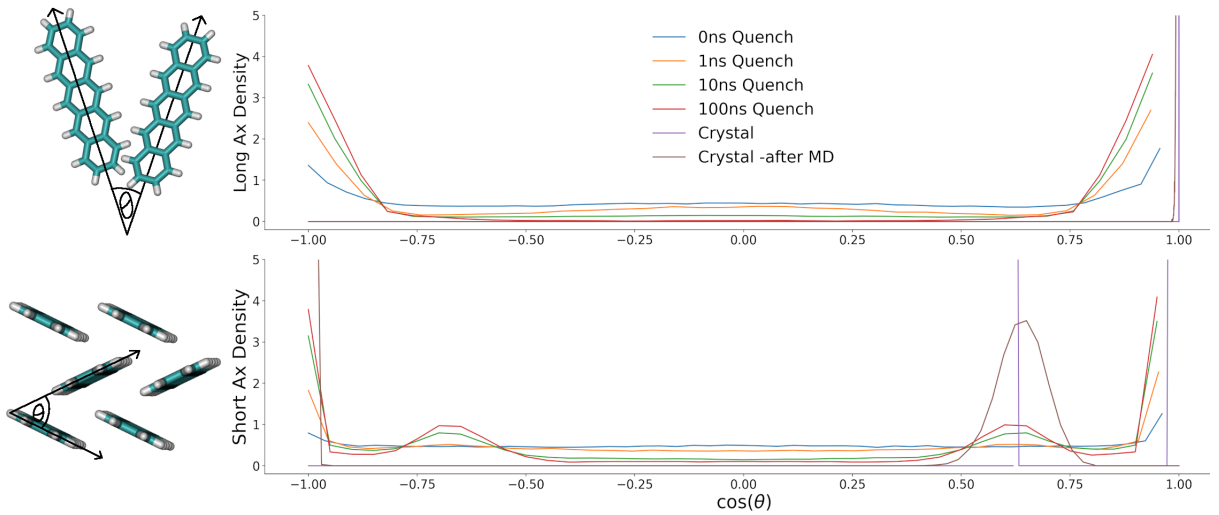


Figure 4.7: The angular distribution for the 4 different quench times is shown above. The brown and purple lines are from a perfect crystal before and after a short MD run. The others are after the various melt-quench simulations. On the right is a schematic showing which angles are referenced in each plot.

The angular distribution shows the distribution angles each molecule makes with the other molecules in the system. In figure 4.7 it was calculated by calculating the angle of an axis of each molecule with its nearest neighbours (a 20Å center of mass cutoff was used). This data was then grouped into a histogram which is plotted. In figure 4.7 we can see as the quenching time increases we start to notice an ever more prominent peak appear at either extreme of the x axis. This is because the molecules are aligning parallel with one another. The symmetry of the plot is an artefact of the melt stage of the simulation where each molecule was free to rotate randomly.

If we now look at the short axis plot we can see that, again, as the quench time increases we start to see a more ordered structure start to form. This time the herringbone

intersection angle between molecules (54.3° ¹⁰⁰) within the herringbone structure is retrieved. This is a result of using partial charges in the simulation -running the same simulations without partial charges results in an unrealistic face-to-face stacking. The brown and purple line show the same calculation run on a crystal of pentacene before and after MD. The purple line comes from an analysis of a repeated unit cell, hence we get 2 delta functions: one at 54.3° and one at 0° . This structure was then equilibrated with electrostatics for 50ps and we start to see a broadening of the herringbone intersection angle and to a lesser extent (on the left side) a broadening of the angle between parallel pairs.

4.2.5 Radial Distribution Function

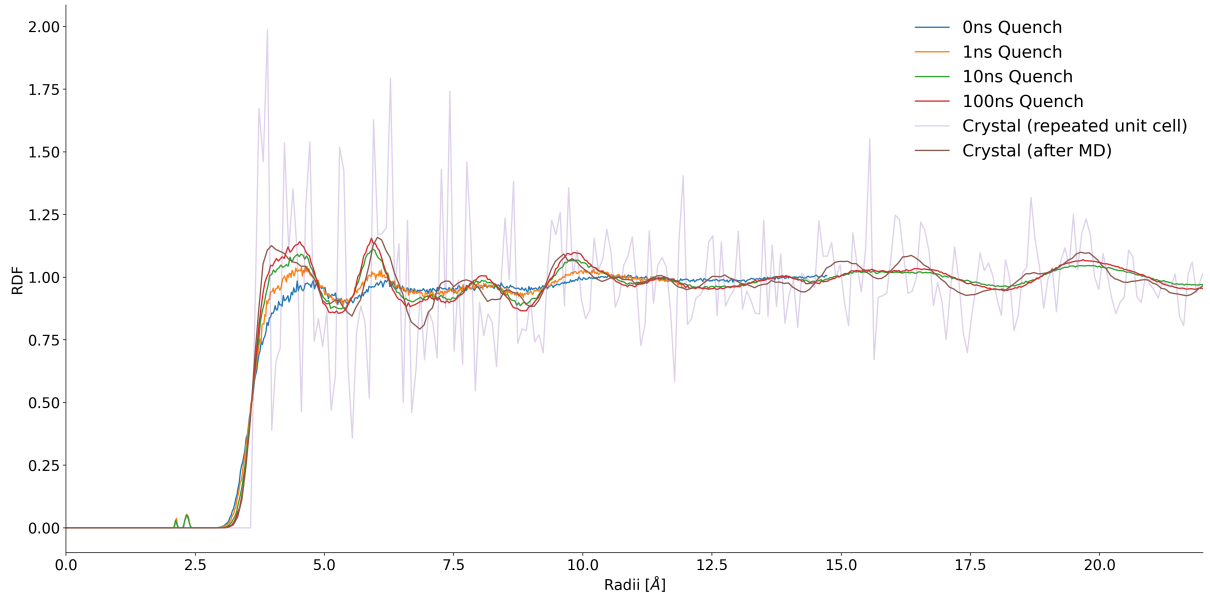


Figure 4.8: The carbon-carbon radial distribution function for 4 different quenching times and a crystal before and after 50ps of MD. The quenches (0, 1, 10 and 100ns) are shown in blue, orange, green and red respectively. The crystal data are shown in purple and brown.

The radial distribution function (RDF) describes the change of density from each particle in the system and is normalised to the bulk density (i.e. $\frac{N}{V}$). This was calculated by counting the number of atoms within a spherical shell from each atom and then dividing by the volume between these spheres. This local density was then normalised to the bulk crystal density. In systems with atoms regularly placed throughout the system we

would expect to see sharp peaks in the RDF as there would be many gaps with no atoms. Conversely, with a totally amorphous system we would expect to see (once we reach twice the Van der Waals radius from each atom) a flat line at 1 as local density should be very similar to the global density. This pattern is what we observe in figure 4.8. The sharp peaks of the purple line show the RDF of a perfect crystal (repeated unit cell) confirming we have a highly ordered system. On the other extreme the blue line shows very weak ordering of the atoms' positions with any ordering vanishing after $\sim 12.5\text{\AA}$ from each atom. This is due to the 0ns structure comprising primarily of small crystal fragments giving rise to a small amount of very local order but over longer distances this order vanishes. Again, as the quench time increases, the ordering increases resulting in larger peaks that more closely match the RDF of the crystal after a short MD equilibration.

4.2.6 Crystallinity

In order to quantify the level of order within the system, an estimator of crystallinity based on the final mass density of the superstructure was used. The formula for this is presented below in equation (4.1)

$$C = 100 \left(\frac{\rho_{sample} - \rho_{amorphous}}{\rho_{crystal} - \rho_{amorphous}} \right) \quad (4.1)$$

This estimator simply linearly interpolates between the minimum (amorphous) density, $\rho_{amorphous}$, and the maximum (crystal) density, $\rho_{crystal}$. The relationship between the quenching time and this definition of crystallinity is shown in figure 4.9. Note in this figure, the quench time 0ns is missing. This is because the system didn't equilibrate instantly and it took approximately 100ps for the density to converge. It can be seen in this figure, that surprisingly, the crystallinity (final density) increases almost exactly logarithmically with respect to quench time. The black dashed line shows a line of best fit using the equation $C = m\log_{10}(t) + C_0$ as a guide for the eye. This crystallinity parameter will be used when looking at the electronic transport properties (hole mobility and IPR) in the following section, in order to compare the electronic transport properties to a physically meaningful property.

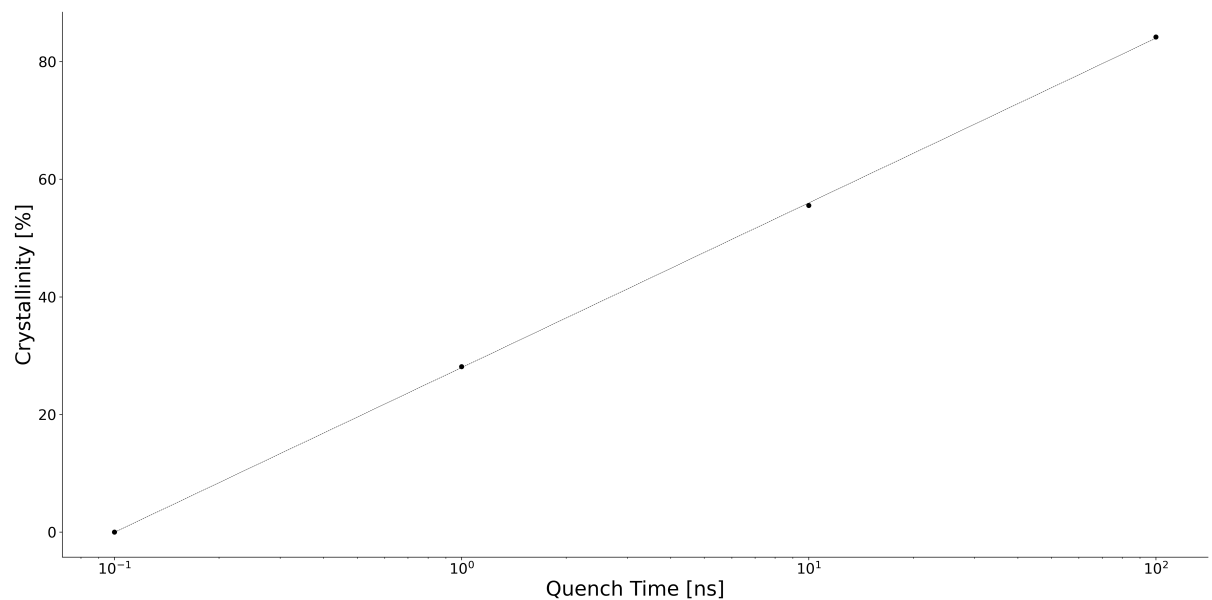


Figure 4.9: The quench time vs crystallinity given by equation 4.1. Black circles show raw data and the dashed black line is a line of best fit using the equation $C = m\log_{10}(t) + C_0$.

4.3 Charge Transfer Properties

We have seen that the final structure of the pentacene systems becomes more ordered and crystal-like as the quenching time is increased. It would be good now to see how this affects the charge transfer properties. A key quantity governing charge transfer rates is the ratio between electronic coupling and reorganisation energy, $\frac{H_{ab}}{\lambda}$. Seeing as we have a single molecule system, by plotting the electronic coupling we can get a qualitative view of the charge transfer dynamics and see which paths are the most likely within the structure.

4.3.1 Global Couplings

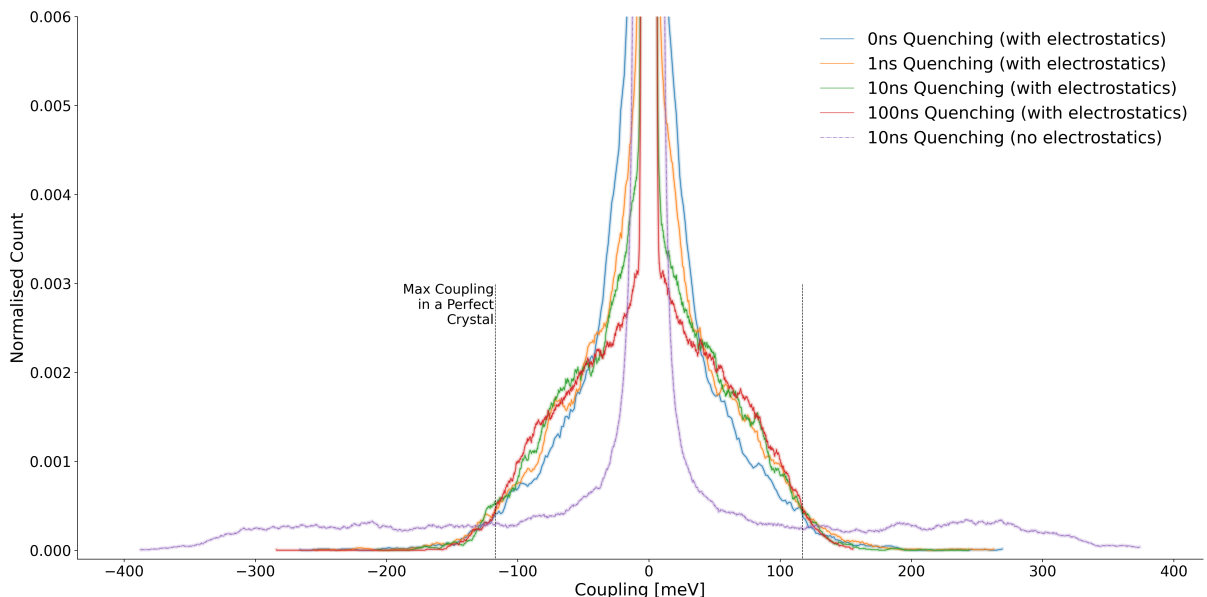


Figure 4.10: The global coupling distribution for each of the quenched structures (in blue, orange, green and red) and 1 structure after a 10ns quench without using electrostatics (purple line). The black dashed lines represent the maximum coupling within a perfect pentacene crystal.

The global coupling distribution gives an overview of the values of coupling within the system, hence an idea of the charge transport properties of the system. To calculate these couplings I have used the analytic overlap method (AOM)⁵⁶ between all pairs of molecules (using a nearest neighbour cutoff) in the final snapshot of each quenched system. As can be seen from figure 4.10, as the quench time increases a knee starts to form in the distribution at a high coupling value (80meV). This is especially obvious in

the 100ns quench structure (red curve) which has far fewer lower energy couplings and more coupling values approaching the crystal maximum of 117meV.

The figure also highlights the importance of a correct account of electrostatic interactions in the formation of these structures. The purple line shows the coupling distribution for the same simulation without any electrostatics. In this curve we see far more very high values of coupling -substantially higher than those seen in the perfect crystal. This is due to it now being energetically favourable to form a more tightly packed face-to-face structures giving rise to larger molecular overlaps hence higher couplings. We see all the other distributions fit well between the 2 black lines, which denote the maximum coupling value in a perfect crystal.

4.3.2 Coupling Networks

In figure 4.11, representative 2D cuts through the samples , corresponding to the areas coloured in gray in Figure 4.9. The centres of mass of each molecule are joined with lines according to the strength of electronic coupling (H_{ab}) between them. Blue, green and red lines depict small, medium and high coupling strengths, $\lambda/100 \leq H_{ab} < \lambda/10$, $\lambda/10 \leq H_{ab} < \lambda/2$ and $\lambda/2 \leq H_{ab}$, respectively, where λ is the molecular (or inner-sphere) reorganization free energy of pentacene, 98 meV. If the picture of hole hopping between molecules was applicable, the blue and green lines would correspond to ET steps in the non-adiabatic and adiabatic regime, respectively. For all red connections, ET theory breaks down because at this point electronic coupling is so strong that there is no longer an activation barrier between initial and final state and the charge carrier starts to de-localize⁷². As expected, it is observed that the sample becomes electronically better connected (more red connections) as the crystallinity increases. This is quantified by clustering regions of high couplings as sets of N molecules that can all be connected with an uninterrupted path of red lines (see Table 4.1 for a summary). In the amorphous sample (0 ns) formation of small islands of size 4 ± 4 molecules begins. At 30% crystallinity these islands become connected resulting in the formation of elongated 1D paths, which extend to 2D clusters at 60% crystallinity. At 80% crystallinity these clusters grow to 9 ± 16 molecules, but still short of the formally infinitely large cluster size of the single

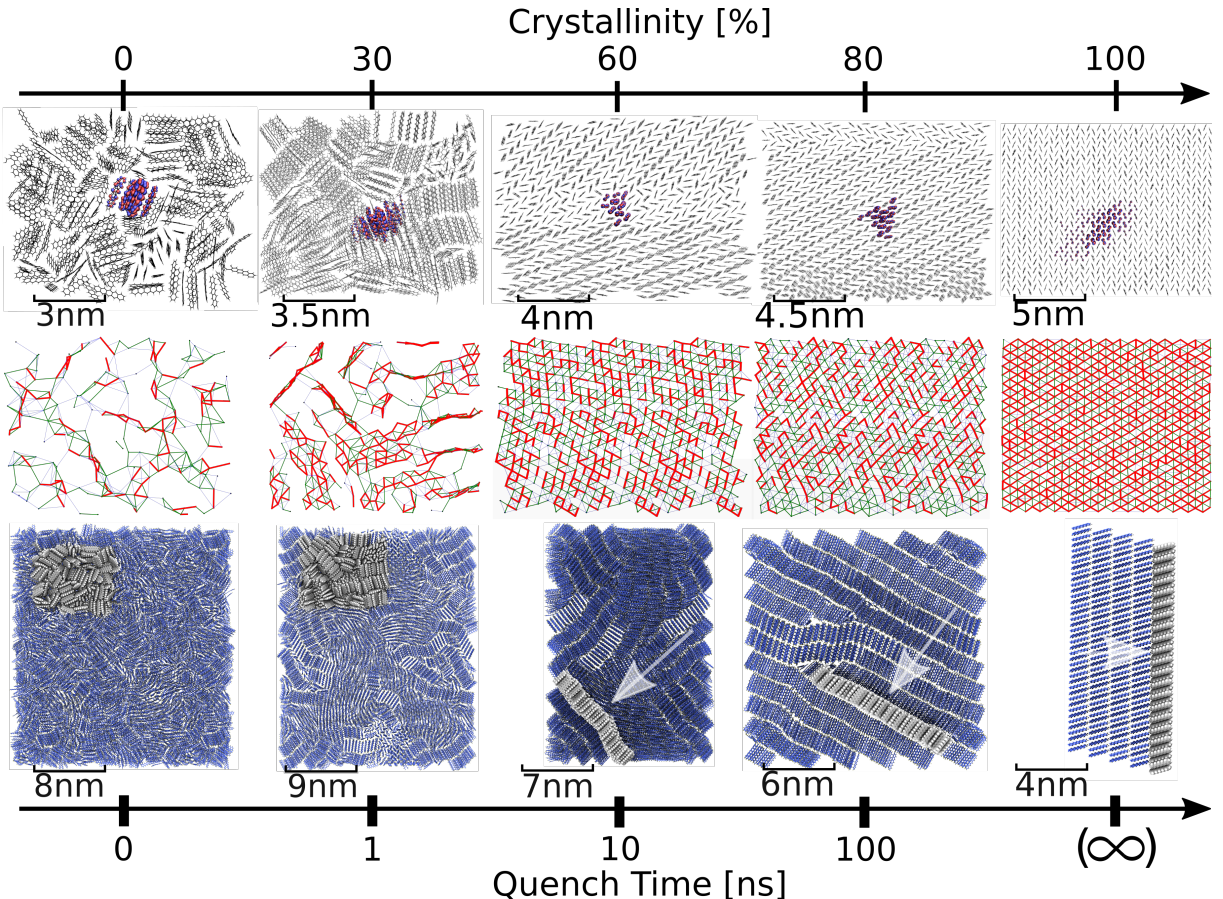


Figure 4.11: Structure and electronic properties of bulk pentacene phases. The disordered structures were obtained from melt-quench molecular dynamics simulation. The bottom row, show a 'front on' view of the entire simulated sample of 3,000 molecules for amorphous and nanocrystalline phases. The final (far-right) image shows the experimental structure of single-crystalline pentacene (polymorph I)¹⁰¹. The region highlighted in light gray, in the following denoted 'active region', is shown enlarged in the middle and bottom rows and viewed 'front on' or as indicated by arrows. The middle row, shows a weighted graph of electronic couplings within the active region. Molecular centers of mass are joined with lines denoting coupling strengths relative to the re-organisation energy of the pentacene molecule. Blue lines depict couplings of $\frac{\lambda}{100} \leq H_{ab} < \frac{\lambda}{10}$, green lines depict couplings of $\frac{\lambda}{10} \leq H_{ab} < \frac{\lambda}{2}$ and red lines depict couplings of $\frac{\lambda}{2} \leq H_{ab}$. The upper row, depicts an isosurface of the hole carrier wavefunction, $\Psi(t)$ (Eq. ??), during FOB-SH simulation of charge transport (red and blue). The crystallinity is an indication of the structural order of the system and was calculated from linearly interpolating between the mass-density of amorphous and single crystalline phases.

crystal. The notably wide spread in cluster size distribution is due to the presence of a large number of smaller clusters (2-4 molecules). This, as will be discussed further below, has a marked impact on electron hole delocalization and mobilities.

Table 4.1: Properties of pentacene in different bulk structures and in ultrathin (2D) films.

τ (ns) ^a	structure ^b	ρ (g cm ⁻³) ^c	bulk pentacene				$\mu^{g,h}$ (comp)	μ^h (exp)	
			Cr (%) ^d	N^e	IPR ^f				
0	am	1.19	0	4±4	3.0	0.21			
1	nc	1.22	30	5±5	3.8	0.23			
10	nc	1.25	60	7±9	4.8	0.92			
100	nc	1.28	80	9±16	9.5	1.8			
(∞)	sc	1.30	100	∞	17	10		5 ⁱ ; 5.6 ^j	
2D pentacene									
	sc, 1L			∞	5.4	4.2		1.6 ^k	
	sc, 2L			∞	12	7.3		3 ^k	

^a Quench time from 800 K to 300 K in molecular dynamics simulation in the NPT ensemble.

^b am = amorphous, nc = nanocrystalline, sc = single crystalline, 1L = 1 wet layer + 1 sc monolayer, 2L = 1 wet layer + sc bilayer.

^c Mass density.

^d Crystallinity, see main text for definition.

^e Mean and root-mean-square fluctuation of number of molecules in clusters with high coupling, see main text.

^f Equation (4.2).

^g Equation (4.6).

^h in units of cm² V⁻¹ s⁻¹.

ⁱ Ref. ¹⁰², OFET, single crystal on Al₂O₃+ionic liquid, polymorph I.

^j Ref. ¹⁰³, OFET, thin single crystal on SiO₂.

^k Ref. ¹⁰⁴, OFET, ultrathin (2D) single crystal on boronitride.

4.4 Surface Hopping Methodology

Several experimental as well as computational studies have indicated that charge transport in crystalline molecular OS falls into a difficult regime where the charge is neither fully delocalised over the bulk material nor completely localised on a single molecule, as had often been assumed.^{105–111} It has recently been shown, using advanced quantum

dynamical simulations, that charge carriers in single-crystalline OS form “flickering polarons”, objects that are half-way between waves and particles^{14,73,112}. It was found they are delocalised over up to 10-20 in the most conductive crystals and constantly change their shape and extension under the influence of the thermal motion of the atoms (crystal vibrations). Taking the example of bulk crystalline pentacene, it was found that the excess hole is typically delocalised over 17 molecules, in excellent agreement with experimental estimates from electron spin resonance data (17 molecules) The delocalisation of the polaron and mobility are limited by the thermal fluctuations of electronic coupling (off-diagonal electron-phonon coupling) and site energy. This picture of charge transport, obtained by numerically solving the time-dependent electronic Schroedinger equation coupled to nuclear motion, resembles closely, and gives support to, the transport scenario predicted by the recently established transient localisation theory (TLT)^{18,19}. However, this makes simulating the charge carrier particularly difficult as the 2 standard techniques (hopping and band theories) breakdown in this regime. Further, TLT is inapplicable to systems with high levels of disorder. For this reason, fragment orbital surface hopping (FOB-SH) was used to simulate the motion of the excess charge carrier in each of the samples and hole-mobilities and inverse participation ratios (IPR) were calculated.

The FOB-SH methodology is a merging of Tully’s original fewest switches surface hopping (described in the introduction) with fragment orbital based framework (described at the beginning of chapter). That is, the Hamiltonian is constructed with diagonals calculated from a classical force-field and off-diagonals calculated from the overlap between singly occupied molecular orbitals (SOMOs). Various extensions to the original surface hopping method have been added to account for overcoherent propagation and trivial crossings leading to spurious transfer. These are mentioned in the introduction and have been discussed at length in various papers^{40,41,69–71,73,74}.

4.4.1 Surface Hopping Setup

The surface hopping simulations require a swarm of hundreds of independent trajectories (~ 500), each with slightly different geometries to fully sample phase space. To create these trajectories, initial positions and velocities were sampled every 1ps from a classical

MD simulation (carried out under NVT). In order to initialise the (electron-hole) wavefunction for each trajectory, the Hamiltonian was calculated. This was then used to find an adiabatic state within $3K_B T$ of the ground state energy, and was relatively close to the center of the simulated system. The details of this procedure are given in appendix H. This initialisation of the wavefunction in a low lying adiabatic state allowed for quick convergence of the mean-squared displacement of the charge carrier. Other parameters, such as the method chosen for correcting for over-coherence, trivial crossings and spurious transfer were taken from previous surface hopping simulations carried out by other members of the Blumberger group. The code at the time did not support the calculation of electrostatic interactions. So, in order to maintain the structure from the melt-quench simulations, center of mass restraints were used. These are shown in appendix ???. Finally, the full system for each of the 4 quench times was very large (3,000 mol). So, to sample the mobility at various points within the superstructure the full system was divided into smaller subsystems. The procedure for dividing the superstructure was different for each quench time and full details are given in appendix J. In the 0ns and 1ns quenched runs, the full system was divided into 6 roughly even slabs. This was because these structures had very little order and the charge transport was expected to be isotropic. In the 10ns and 100ns quenched systems, a DBSCAN-like algorithm¹¹³ was used to cluster molecules (by mass-density). These clusters were then used as active regions within the surface hopping code.

4.4.2 Inverse Participation Ratio

The inverse participation ratio (IPR) gives a measure of spread of the polaron. A value of 1 would mean the polaron is localised on a single molecule, a completely delocalised polaron would have a value of N_{mol} where N_{mol} is the number of molecules in the system. The formula used in its calculation is given below in equation (4.2):

$$IPR(t) = \frac{1}{N_{\text{traj}}} \sum_{n=1}^{N_{\text{traj}}} \frac{1}{\sum_i^{N_{\text{mol}}} |u_i^n(t)|^4} \quad (4.2)$$

Where N_{traj} (mol) represents the number of trajectory (molecules) and $u_i^n(t)$ is the diabatic expansion coefficient at time t , on replica n and molecule i .

The IPR is an important quantity as the level of delocalisation of the wavefunction is positively correlated with its mobility. That is, molecular systems that have a large delocalisation of the charge carrier tend to have larger mobilities. It is also useful in determining if the system has reached equilibrium, as in equilibrium the IPR tends to converge to a constant value.

4.4.3 Hole Mobilities

A full discussion of the calculation of the charge carrier mobility can be found in various papers^{14,40?}. It is calculated from the Einstein diffusion constant, D , which in turn is calculated from the change in the mean squared displacement (MSD) of the charge carrier. The MSD is calculated via equation (4.4) below

$$MSD_{ab}(t) = \frac{1}{N_{\text{traj}}} \sum_{n=1}^{N_{\text{traj}}} \langle \Psi^n(t) | (\mathbf{R} - \mathbf{R}_0)^2 | \Psi^n(t) \rangle \quad (4.3)$$

$$\approx \frac{1}{N_{\text{traj}}} \sum_{n=1}^{N_{\text{traj}}} \left(\frac{1}{\sum_i^{N_{\text{mol}}}} |u_i^n(t)|^2 (\mathbf{R}_i^n(t))^2 \right) \quad (4.4)$$

Where Ψ^n is the wavefunction for trajectory n , \mathbf{R} is the position coordinate and \mathbf{R}_0 is the position coordinate at time $t = 0$. $\mathbf{R}_i^n(t)$ is the time-dependent position of the center of mass of molecule i on trajectory n . Equation (4.3) is the exact quantum mechanical equation for the MSD, equation (4.4) is the equation that is used to calculate the MSD from the surface hopping output. The quantity is in general a 3x3 matrix and the values a and b are indices indexing each of the 3 Cartesian dimensions.

After a small equilibration the MSD increases linearly. This is indicative of Einstein diffusion and the coefficient can be calculated, in this linear regime, as in equation (4.5) below:

$$D_{ab} = \frac{1}{2} \lim_{t \rightarrow \infty} \frac{d}{dt} MSD_{ab}(t) \quad (4.5)$$

In order to calculate the time-derivative of the MSD, a line of best-fit is fitted to the MSD vs simulation time and the gradient is calculated. This is then used in the calculation of

the mobility in equation (4.6) below.

$$\mu_{ab} = \frac{eD_{ab}}{k_B T} \quad (4.6)$$

Where k_B is the Boltzmann constant, e the elementary charge and T is the temperature. The charge mobility is a quantity that can be calculated in experimental studies, so is an important quantity to calculate. It shows how quickly charge can be transported across a system and can be used to calculate other important quantities such as drift velocity ($v_d = \mu E$) or conductivity ($\sigma \propto \mu N_{carrier}$).

4.4.4 Surface Hopping Results

4.4.4.1 Quantum Localisation

The IPR is plotted, along with the hole mobility, in figure 4.12 for the amorphous, nanocrystalline and single crystalline samples. It is clearly visible that the delocalisation of the carrier wavefunction, defined in terms of the inverse participation ratio (IPR, Eq. ??), increases with increasing crystallinity, reflecting the trend seen in the electronic coupling maps. In the amorphous sample, the static disorder of electronic coupling results in the wavefunction localising, on average, over just 2-3 molecules. At 30% and 60% crystallinity, the high concentration of defects restricts wavefunction delocalisation over 5-6 molecules, whereas at 80% we observe a marked increase to 10 molecules, which is still some way off from the value for the single crystal, 17 molecules. At this point we also see for the first time a clear spatial anisotropy of the charge carrier wavefunction extending more strongly along the T1 high coupling direction in the pentacene crystal (diagonal direction in Figure 4.9). Remarkably, we notice a good correlation between the IPR and the cluster size in the electronic coupling map (Table ??) suggesting that carrier delocalisation is limited by static disorder of electronic coupling. This correlation is lost for the single crystal because in this case delocalisation is limited by the thermal disorder of electronic couplings (i.e., dynamic or electron-phonon coupling).

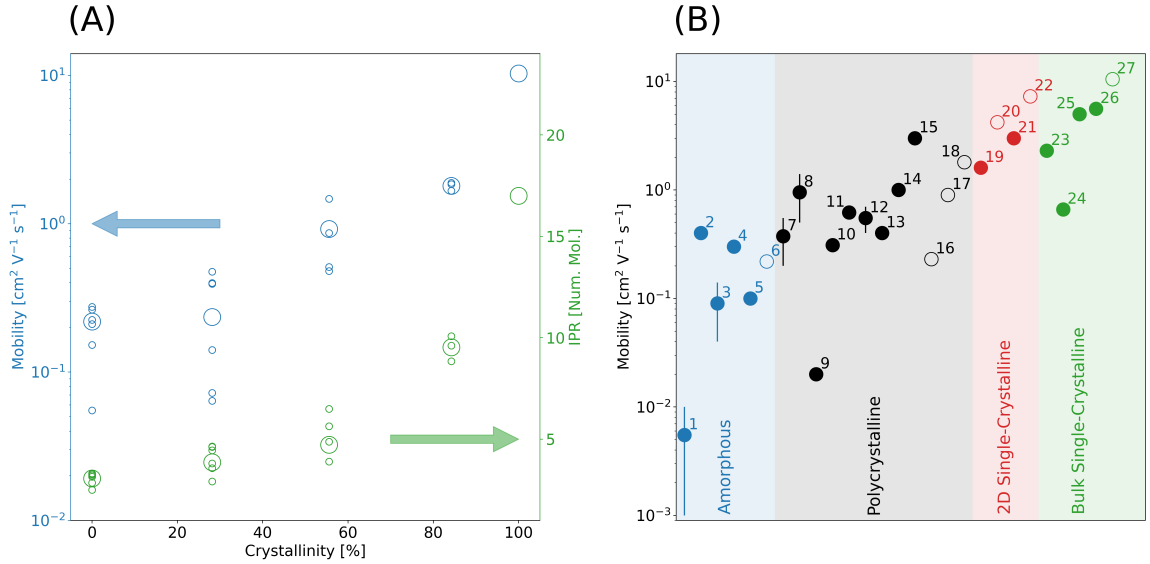


Figure 4.12: Hole mobilities and inverse participation ratio (IPR) for the pentacene phases studied. In (A), computed hole mobilities and IPR from FOB-SH simulation are shown for bulk pentacene phases as a function of the crystallinity of the sample (blue and green circles, respectively). The local mobilities and IPR for different regions of the sample are shown in small circles and the averages are shown in large circles. In (B), computed mobilities (blue) for bulk pentacene phases and 2D pentacene layers (blue symbols) are compared to experimental results (black symbols). The bulk pentacene phases were classified as ‘amorphous’, ‘polycrystalline’ and single-crystalline. Error bars for computed values indicate the spread in local mobility. 1,2: ref. ¹¹⁴, 3: ref. ¹¹⁵, 4,5: ref. ¹¹⁶, 6: this work, $Cr = 0\%$, 7,8: ref. ¹¹⁷, 9,10,11: ref. [?], 12: ref. [?], 13,14,15: ref. [?], 16: this work, $Cr = 30\%$, 17: this work, $Cr = 60\%$, 18: this work, $Cr = 80\%$, 19: ref. ¹⁰⁴, 20: this work, 2D pentacene, 1L, 21: ref. ¹⁰⁴, 22: this work, 2D pentacene, 2L, 23,24: ref. [?], 25: ref. ¹⁰², 26: ref. ¹⁰³, 27: this work, $Cr = 100\%$. Additional information on the device measurements and gate dielectrics used can be found in appendix K, Table K.1.

4.4.4.2 Hole Mobilities

Hole mobilities for all samples were obtained as explained in section 4.4.3. For each superstructure multiple active regions were selected to calculate a mobility for. These “local” charge mobilities can show the impact of structural inhomogeneity of the quenched samples on charge transport. We find that in the disordered samples, especially the one with $\sim 30\%$ crystallinity, the local charge mobilities and IPR values exhibit a relatively large spread as some regions are more crystalline and thus more conductive than others (Figure 4.12, small open circles). In the structurally more homogenous sample with 80% crystallinity, the variation in local mobility becomes almost negligible. The average of the

local charge mobilities and IPRs correlate well with the crystallinity of the sample (Figure 4.12, large circles). Over the last 20 years a large number of experimental hole mobilities have been reported for pentacene thin films and crystals from organic field effect transistor (OFET) measurements. Yet, there are several issues to consider when comparing our calculations to these measurements. In OFETs charge transport is typically probed on the micrometer scale over macroscopic time scales, whereas present calculations are carried out for nanoscale samples over short times (ps-ns). Moreover, OFET mobilities have been shown to be very sensitive to many details of the preparation method including, e.g., the gate dielectric used, the surface roughness, deposition rate and temperature etc. This can be seen in the very large spread of experimental mobilities for amorphous pentacene (figure 4.12, solid pentagons). My calculated value of hole mobility, of $0.14 \text{ cm}^2 \text{ V}^{-1} \text{ s}^{-1}$, fits towards to upper end of this spread. It is suspected that the inclusion of electrostatic interactions may reduce this further. This may be due to increased trapping of the polaron from larger levels of energetic disorder (larger site energy differences in the language of FOB-SH). That is the inclusion of electrostatics is thought to increase the energy penalty from transitioning from an initial state with N_{init} states charged to the final state with N_{final} states charged. It is not thought that these extra interactions would affect the more crystalline systems, as contrary to the amorphous case, each molecule feels a very similar electrostatic potential due to the very ordered nature of the structure. A fuller discussion of the role of electrostatics can be seen in Martinelli et al¹¹⁸.

Notwithstanding the above caveats, the correlation between experiment and computed FOB-SH mobilities is rather good, which supports the mechanistic picture that our simulations have revealed. The simulated results have been compared to experimental values for the fully amorphous and fully crystalline samples. For the fully crystalline sample the agreement to experiment is very good, our simulations produced a value of $10.3 \text{ cm}^2 \text{ V}^{-1} \text{ s}^{-1}$ whereas experimental studies have reported values ranging from $5\text{-}10.5 \text{ cm}^2 \text{ V}^{-1} \text{ s}^{-1}$. Again the value reported in this work sits at the upper end of the experimentally reported values for reasons discussed previously.

4.5 Conclusions

In this chapter, I have presented a molecular dynamics method for tuning the crystallinity of a pentacene sample based on melting and subsequently quenching the sample over various timescales. I have shown, as was expected, that longer quench times lead to more ordered structures and discussed the mechanism leading to this. That is, in longer quench times the few crystal fragments that begin to seed have a longer time to grow before their growth is impeded by neighbouring crystal fragments. I have displayed various macroscopic properties that confirm that the longer quench times do indeed show more order, including mass-density, angular distribution and the radial distribution function. Further, I have presented networks of electronic coupling within each of the quenched systems, that can be used to get a qualitative feel for the electronic transport properties without expensive quantum dynamics simulations.

In calculating quantitative values for hole mobilities to compare to experimental values, I have shown that it is now possible to use explicit quantum dynamical calculations to simulate charge carrier transport in large, realistic samples of disordered organic semiconductors. My results are in remarkably good agreement with those available from experiment and provide a molecular-scale picture of the Nature of the charge carrier and the transport mechanism as a function of the crystallinity of the system. The notion that charge carrier transport in disordered systems occurs via small polaron hopping is shown to be a reasonably good approximation only for fully amorphous systems - for semi-crystalline and crystalline samples significant charge carrier delocalization occurs mandating the use of more advanced transport simulations, e.g. the FOB-SH method used here. In general, there is a good correlation between crystallinity, carrier delocalization and mobility. Interestingly, we find that even relatively small amounts of structural disorder can lead to a significant drop in charge carrier delocalization and hole mobility compared to the single crystal. This is an important consideration when comparing charge carrier mobilities in simulated organic systems, usually perfectly crystalline, with those of experiment, where it is difficult to prepare highly pure crystals devoid of defects. This approach is generally applicable to any molecular organic semiconductor and may

be used for identifying new disordered materials with high charge mobility.

Finally, this study has served to highlight a potential drawback in the FOB-SH methodology as it currently stands. That is, the lack of electrostatic interactions within the simulations. These have not been implemented previously as the group's work was focussed on perfect crystals, where electrostatic interactions are not expected to affect the final result. However, in the more disordered systems this approximation may be a step too far. In the final chapter of this thesis, I will present my implementation of electrostatics within the surface hopping and a possible alternative to expensive Ewald summation.

Appendix A

Tully Model Paramters

A.1 Model 1 -Single Avoided Crossing

	Quantity	Value	Unit
Hamiltonian Paramters:			
$H_{11}(\mathbf{R}) = A \tanh(B\mathbf{R})$	Initial Position	-20	a.u.
$H_{12}(\mathbf{R}) = Ce^{-D\mathbf{R}^2}$	Initial Velocities	15.0, 25.0	a.u.
$H_{21}(\mathbf{R}) = H_{12}(\mathbf{R})$	Initial Adiab Pop	ground state	-
$H_{22}(\mathbf{R}) = -H_{11}(\mathbf{R})$	Simulation Time	6000, 4000	a.u.
Where $A = 0.03$, $B = 0.4$, $C = 0.005$ and $D = 0.3$	$\sigma_v^{(I)}$	0.5	a.u.
	M (σ constant)	40	-
	$\Delta t_{\text{nuclear}}$	0.1	fs
	$\Delta t_{\text{electronic}}$	0.01	fs
	$\frac{\delta \mathbf{R}_{lk,v}^{(I)}}{\delta t}$ threshold	0.15	a.u.
	N_{rep}	200	-

A.2 Model 2 -Dual Avoided Crossing

	Quantity	Value	Unit
Hamiltonian Paramters:			
$H_{11}(\mathbf{R}) = 0$	Initial Position	-8	a.u.
$H_{12}(\mathbf{R}) = Ce^{-D\mathbf{R}^2}$	Initial Velocities	16.0, 30.0	a.u.
$H_{21}(\mathbf{R}) = H_{12}(\mathbf{R})$	Initial Adiab Pop	ground state	-
$H_{22}(\mathbf{R}) = -Ae^{-B\mathbf{R}^2} + E$	Simulation Time	2500, 1500	a.u.
Where A = 0.1, B = 0.28, C = 0.015, D = 0.06 and E = 0.05	$\sigma_v^{(I)}$	0.5	a.u.
	M (σ constant)	40	-
	$\Delta t_{\text{nuclear}}$	0.1	fs
	$\Delta t_{\text{electronic}}$	0.01	fs
	$\frac{\delta \mathbf{R}_{ik,v}^{(I)}}{\delta t}$ threshold	0.15	a.u.
	N_{rep}	200	-

A.3 Model 3 -Extended Coupling

	Quantity	Value	Unit
Hamiltonian Paramters:			
$H_{11}(\mathbf{R}) = A$	Initial Position	-15	a.u.
$H_{12}(\mathbf{R}) = \begin{cases} Be^{C\mathbf{R}}, & R \leq 0 \\ B(2 - e^{-C\mathbf{R}}), & R > 0 \end{cases}$	Initial Velocities	10, 30	a.u.
$H_{21}(\mathbf{R}) = H_{12}(\mathbf{R})$	Initial Adiab Pop	ground state	-
$H_{22}(\mathbf{R}) = -H_{11}(\mathbf{R})$	Simulation Time	5000, 1500	a.u.
Where A = 6×10^{-4} , B = 0.1 and C = 0.9	$\sigma_v^{(I)}$	0.5	a.u.
	M (σ constant)	40	-
	$\Delta t_{\text{nuclear}}$	0.1	fs
	$\Delta t_{\text{electronic}}$	0.01	fs
	$\frac{\delta \mathbf{R}_{ik,v}^{(I)}}{\delta t}$ threshold	0.15	a.u.
	N_{rep}	200	-

A.4 Model 4 -Dual Arch

Hamiltonian Paramters:

$$\begin{aligned}
 H_{11}(\mathbf{R}) &= A \\
 H_{12}(\mathbf{R}) &= \begin{cases} B \left[-e^{C(\mathbf{R}-D)} + e^{C(\mathbf{R}+D)} \right] & R \leq -D \\ B \left[e^{-C(\mathbf{R}-D)} - e^{-C(\mathbf{R}+D)} \right] & R \geq D \\ B \left[2 - e^{C(\mathbf{R}-D)} - e^{-C(\mathbf{R}+D)} \right] & -D < R < D \end{cases} \\
 H_{21}(\mathbf{R}) &= H_{12}(\mathbf{R}) \\
 H_{22}(\mathbf{R}) &= -H_{11}(\mathbf{R})
 \end{aligned}$$

Where $A = 6 \times 10^{-4}$, $B = 0.1$, $C = 0.9$ and

$D = 4$

Quantity	Value	Unit
Initial Position	-20	a.u.
Initial Velocities	10, 40	a.u.
Initial Adiab Pop	ground state	-
Simulation Time	6000, 2000	a.u.
$\sigma_v^{(I)}$	0.5	a.u.
M (σ constant)	40	-
$\Delta t_{\text{nuclear}}$	0.1	fs
$\Delta t_{\text{electonic}}$	0.01	fs
$\frac{\delta \mathbf{R}_{lk,v}^{(I)}}{\delta t}$ threshold	0.15	a.u.
N_{rep}	200	-

Appendix B

Wigner Distribution Derivation

The nuclear wavepacket (at time 0) is given by:

$$\chi(R) = \frac{1}{(\pi\mu^2)^{\frac{1}{4}}} e^{-\frac{(R-R_0)^2}{2\mu^2} + ik_0(R-R_0)} \quad (\text{B.1})$$

The Wigner quasiprobability function for momentum and position (p, R) is given by:

$$W(p, R) = \frac{1}{\pi\hbar} \int_{-\infty}^{\infty} \chi^*(R+y)\chi(R-y)e^{\frac{2ipy}{\hbar}} dy \quad (\text{B.2})$$

However, both Ehrenfest and CTMQC require atomic positions as input so we must extract the position and velocity probability densities from this. We get these from the marginal integrals of the Wigner distribution i.e.

$$|f(R)|^2 = \int_{-\infty}^{\infty} W(R, p) dp \quad (\text{B.3})$$

$$|f(p)|^2 = \int_{-\infty}^{\infty} W(R, p) dR \quad (\text{B.4})$$

In order to calculate these marginal integrals we must first crunch through the maths of equation (B.2). Substituting eq (B.1) into (B.2):

$$W(p, R) = \frac{1}{\pi\hbar} \int_{-\infty}^{\infty} \frac{1}{\mu\sqrt{\pi}} e^{-\frac{(R+y-R_0)^2}{2\mu^2} - 2ik_0y - \frac{(R-y-R_0)^2}{2\mu^2}} e^{\frac{2ipy}{\hbar}} dy \quad (\text{B.5})$$

Simplifying the 2 quadratic equations (equation (B.5)) we get:

$$W(p, R) = \frac{1}{\pi \hbar} \int_{-\infty}^{\infty} \frac{1}{\mu \sqrt{\pi}} e^{-\mu^{-2}(y^2 - 2ik_0 y \mu^2 + (R-R_0)^2)} e^{\frac{2ipy}{\hbar}} dy \quad (\text{B.6})$$

We can now take the expressions not dependant on y outside of the integral and combine the exponents.

$$W(p, R) = \frac{1}{\pi \sqrt{\pi} \mu \hbar} e^{-\frac{(R-R_0)^2}{\mu^2}} \int_{-\infty}^{\infty} e^{-\frac{y^2 + 2iy\mu^2(\frac{p}{\hbar} - k_0)}{\mu^2}} dy \quad (\text{B.7})$$

Integrating we get:

$$\int e^{-\frac{y^2 + 2iy\mu^2(\frac{p}{\hbar} - k_0)}{\mu^2}} dy = \frac{\sqrt{\pi} \mu}{2} e^{-\frac{\mu^2}{\hbar^2}(p - \hbar k_0)^2} \operatorname{erf} \left[\frac{y}{\mu} + i \left(\frac{p\mu}{\hbar} - \mu k_0 \right) \right] \quad (\text{B.8})$$

Applying limits we get:

$$\int_{-\infty}^{\infty} e^{-\frac{y^2 + 2iy\mu^2(\frac{p}{\hbar} - k_0)}{\mu^2}} dy = \sqrt{\pi} \mu e^{-\frac{\mu^2}{\hbar^2}(p - \hbar k_0)^2} \quad (\text{B.9})$$

Substituting this back into the Wigner distribution (equation (B.2)) we finally get:

$$W(p, R) = \frac{1}{\pi \hbar} e^{-\frac{(R-R_0)^2}{\mu^2}} e^{-\frac{(p - \hbar k_0)^2}{\hbar^2/\mu^2}} \quad (\text{B.10})$$

Taking the marginal integrals we get the position and velocity probability distributions:

$$|f(R)|^2 = \frac{2}{\mu \sqrt{\pi}} e^{-\frac{(R-R_0)^2}{\mu^2}} \quad (\text{B.11})$$

$$|f(p)|^2 = \frac{2}{\frac{\hbar}{\mu} \sqrt{\pi}} e^{-\frac{\mu^2}{\hbar^2}(p - \hbar k_0)^2} \quad (\text{B.12})$$

The above distributions are randomly sampled to get initial atomic velocities and positions for each simulation.

Appendix C

$\mathbf{R}_{lk,v}$ Alternatives

C.1 $\mathbf{R}_{lk,v}$ Extrapolation

C.2 Alternative Quantum Momentum Intercept

In Agostini, 16² another quantum momentum intercept term is discussed. This term is not used because, as previously discussed in section 1.4, it leads to unphysical transfer of population between adiabatic states when the nonadiabatic coupling elements are 0. However, it can be used in these Tully Models as an effective fix to the discontinuities caused by the $\mathbf{R}_{lk,v}$ term.

The other quantum momentum intercept, $\mathbf{R}_{0,v}^{(I)}$, comes directly from the construction of the nuclear density using a linear combination of a product of gaussians (see equation (1.14) in the introduction). It is defined as in equation (C.1) below:

$$\mathbf{R}_{0,v}^{(I)} = \sum_{J}^{N_{tr}} \left[\frac{\hbar \prod_{v'} g_{\sigma_{v'}^{(J)}(t)} \left(\mathbf{R}_{v'}^{(I)}(t) - \mathbf{R}_{v'}^{(J)}(t) \right)}{2 \sigma_v^{(J)}(t)^2 \sum_{K}^{N_{tr}} \prod_{v'} g_{\sigma_{v'}^{(K)}(t)} \left(\mathbf{R}_{v'}^{(I)}(t) - \mathbf{R}_{v'}^{(K)}(t) \right)} \mathbf{R}_v^{(I)} \right] \quad (\text{C.1})$$

However, as switching to this intercept directly may cause discontinuities in itself a smoothing parameter is applied to ease the switch. This is given in equation (C.2) below:

$$[1 - A(t)] R_{good}(t) + A(t) R_{bad}(t) = R_{effective}(t) \quad (\text{C.2})$$

R_{good} refers to the intercept that should be switched to (e.g. for the detection of a spike in the $R_{lk,v}^{(I)}$ we switch to the intercept in in equation (C.1)). $R_{lk,v}^{(I)}$ refers to the intercept that is being switched from (e.g. when it is detected that the divergence of $R_{lk,v}^{(I)}$ has finished then we switch from the alternative intercept back to $R_{lk,v}^{(I)}$). $A(t)$ is a smoothing parameter and is given in equation (C.3) below:

$$A(t) = \frac{D_v^{(I)}}{2} \left[\tanh\left(t - \frac{t_{final} + t_{init}}{0.6Ndt}\right) + 1 \right] \quad (\text{C.3})$$

Where $D_v^{(I)}$ is the distance between the 2 intercepts (e.g. $D_v^{(I)} = R_{lk,v}^{(I)} - R_{0,v}^{(I)}$), N is the number of steps to take before settling solely on one intercept, t_{init} is the time of detection of the divergence, t_{final} is the time at which the code settles on 1 intercept and dt is the timestep taken.

A cartoon of this process is given in figure C.1

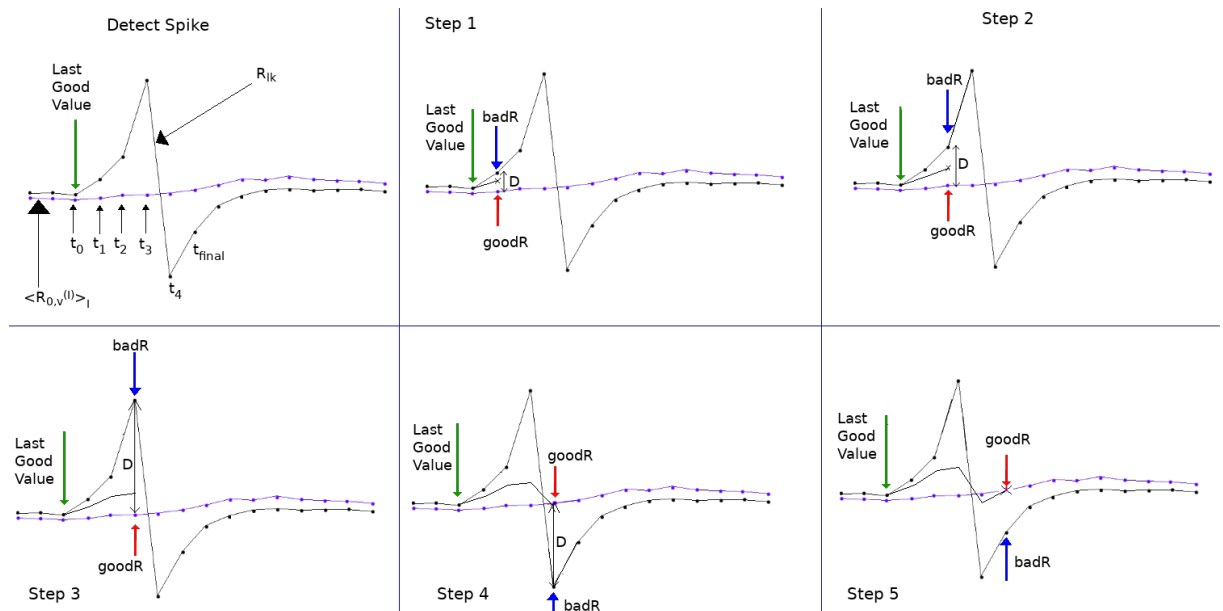


Figure C.1: A crude demonstration of the principle behind the smoothing procedure in switching between intercepts. The black line shows an intercept begin to diverge and the alternative intercept is shown in purple. As the step is incremented the amount of the alternative intercept that makes up the effective intercept is increased until only 1 intercept is used.

Appendix D

Rabi Oscillation

The time dependant Schrödinger equation is given below:

$$\hbar \frac{\delta}{\delta t} \Phi(\mathbf{R}(t), t) = \hat{H}(\mathbf{R}(t), t) \Phi(\mathbf{R}(t), t) \quad (\text{D.1})$$

If we hold the nuclear coordinates in place (e.g. remove time-dependence from nuclear coordinates) we get an ordinary differential equation as shown below:

$$\hbar \frac{d}{dt} \Phi(\mathbf{R}, t) = \hat{H}(\mathbf{R}, t) \Phi(\mathbf{R}, t) \quad (\text{D.2})$$

This has the following general solution. This can be solved with a Taylor series expansion.

$$\Phi(\mathbf{R}, t) = e^{\hbar \hat{H} t} \Phi(\mathbf{R}, 0)$$

Figure

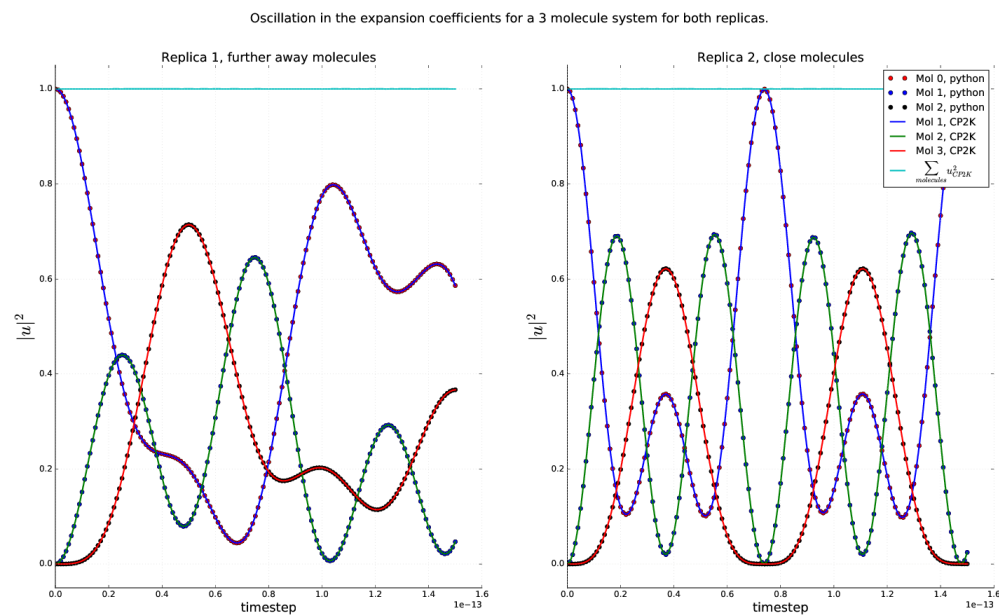


Figure D.1: Rabi oscillation occurring within a Ethylene trimer system. Dotted lines were calculated using equation (D.2), solid lines were calculated using the RK4 propagator within the CTMQC section of the CP2K code. The norm is shown on the top as a cyan line and the x axis shows the timestep in seconds.

Appendix E

Norm Conservation in CTMQC and Ehrenfest

A statement of the conservation of the norm, for a single trajectory, is given below in equation (E.1)

$$\frac{d}{dt} \sum_l |C_l(t)|^2 = \sum_l C_l^*(t) \frac{dC_l(t)}{dt} + \frac{dC_l^*(t)}{dt} C_l(t) = 2\mathbb{R} \left[\sum_l C_l(t)^* \frac{dC_l(t)}{dt} \right] \quad (\text{E.1})$$

Substituting the equation for the evolution of the adiabatic coefficients (and removing the purely imaginary term) into (??) we get equation (E.3)

$$\frac{d}{dt} \sum_l |C_l(t)|^2 = 2 \sum_l \mathbb{R} \left[\frac{-i}{\hbar} \cancel{\epsilon_{B\theta}^l} C_l(t)^* \cancel{C_l(t)} - \sum_k \left[C_l(t)^* C_k(t) d_{lk}^{ad} - (A_l - B_l) C_l(t)^* C_l(t) \right] \right] \quad (\text{E.2})$$

$$= -2 \sum_l \mathbb{R} \left[\sum_k \left[C_l(t)^* C_k(t) d_{lk}^{ad} - (A_l - B_l) C_l(t)^* C_l(t) \right] \right] \quad (\text{E.3})$$

Where:

$$A_l = \sum_{v=1}^{N_n} \sum_k \frac{\mathcal{Q}_{lk,v}(t)}{\hbar M_v} \cdot \mathbf{f}_{k,v}(t) |C_k(t)|^2 \quad (\text{E.4})$$

$$B_l = \sum_{v=1}^{N_n} \sum_k \frac{\mathcal{Q}_{lk,v}(t)}{\hbar M_v} \cdot \mathbf{f}_{l,v}(t) |C_k(t)|^2 \quad (\text{E.5})$$

The NACE term evaluates to 0 due to the anti-symmetry of the NACE giving us equation (E.7).

So far, we have proved that the norm should be conserved here for all terms apart from the quantum momentum terms i.e. Ehrenfest.

$$\frac{d}{dt} \sum_l |C_l^{QM}(t)|^2 = 2 \sum_l \Re[(A_l - B_l) C_l(t)^* C_l(t)] \quad (\text{E.6})$$

$$= 2 \left[\sum_l A_l |C_l(t)|^2 - \sum_l B_l |C_l(t)|^2 \right] \quad (\text{E.7})$$

However, $\sum_l A_l |C_l|^2 \equiv \sum_l B_l |C_l|^2$, therefore there is no change in the population and the norm should be conserved.

Appendix F

Dynamic σ Calculation

The algorithm for dynamically updating the σ parameter outlined in Gossel, 18³ is provided below.

1. Set an initial width parameter ($\sigma_v^{(I)}(t - dt)$) and a constant we will name D .
2. Calculate a cutoff distance via: $r_{cut}(t) = D\sigma_v^{(I)}(t - dt)$.
3. For each atom index, v , and replica, I , gather replicas within a cutoff distance of the current replica. Set the number of replicas within the cutoff distance to N .
4. Calculate the distance between atoms on different replicas.
5. Find the standard deviation of these distances and set the width of the gaussian, centered on atom v and replica I , to this standard deviation.
6. If the standard deviation is smaller than $\frac{D}{N} \min_I [\sigma_v^{(I)}(t - dt)]$ then set $\sigma_v^{(I)}(t) = \frac{D}{N} \min_I [\sigma_v^{(I)}(t - dt)]$.

Appendix G

Basis Transformation

We can expand the Schrödinger equation in terms of a diabatic basis, ϕ rather than an adiabatic one, ψ . These 2 expansions are given in equations (G.1) and (G.2).

$$|\Psi\rangle = \sum_n C_n |\psi_n\rangle \quad (\text{G.1})$$

$$|\Psi\rangle = \sum_l u_l |\phi_l\rangle \quad (\text{G.2})$$

It follows from this we can define a transformation matrix, U_{ln} to transform between the adiabatic and diabatic bases. This is shown in equation (G.3) where the $\overset{\leftrightarrow}{I}$ symbol represents the identity matrix. This identity only holds in the orthogonal diabatic basis ϕ and wouldn't hold for non-orthogonal bases.

$$|\psi_n\rangle = \overset{\leftrightarrow}{I} |\psi_n\rangle = \sum_l |\phi_l\rangle \langle \phi_l| \psi_n\rangle = \sum_l |\phi_l\rangle U_{ln} \quad (\text{G.3})$$

A similar relation between expansion coefficients exists

$$\sum_n C_n |\psi_n\rangle = \sum_l u_l |\phi_l\rangle \quad (\text{G.4})$$

$$\sum_n C_n \langle \psi_m | \psi_n \rangle = \sum_l u_l \langle \psi_m | \phi_l \rangle \quad (\text{G.5})$$

$$C_m = \sum_l u_l U_{lm}^* \quad (\text{G.6})$$

Finally an important property of the transformation matrix is given in equation (G.7).

$$\sum_m U_{im} U_{lm}^* = \sum_m \langle \phi_i | \psi_m \rangle \langle \psi_m | \phi_l \rangle = \langle \phi_i | \phi_l \rangle = \delta_{il} \quad (\text{G.7})$$

Equations (G.3), (G.6) and (G.7) will be used below to transform the propagation equations from the adiabatic basis to the diabatic one.

G.1 Forces

The equation for the propagation of the forces in the adiabatic basis is:

$$\begin{aligned} \mathbf{F}_v^{(I)} = & - \sum_n |C_n^{(I)}|^2 \nabla_v E_n^{(I)} - \sum_{n,m} C_m^{*(I)} C_n^{(I)} \left(E_n^{(I)} - E_m^{(I)} \right) \mathbf{d}_{v,mn}^{ad,(I)} \\ & - \sum_{m,n} |C_m^{(I)}|^2 \left(\sum_{v'}^{N_n} \frac{2}{\hbar M_{v'}} \mathcal{Q}_{v',mn}^{(I)} \cdot \mathbf{f}_{m,v'}^{(I)} \right) [\mathbf{f}_{n,v}^{(I)} - \mathbf{f}_{m,v}^{(I)}] |C_n^{(I)}|^2 \end{aligned} \quad (\text{G.8})$$

The quantum momentum part of the equation cannot be easily transformed so this will focus on the Ehrenfest part:

$$\mathbf{F}_{eh,v}^{(I)} = - \sum_n |C_n^{(I)}|^2 \nabla_v E_n^{(I)} - \sum_{n,m} C_m^{*(I)} C_n^{(I)} \left(E_n^{(I)} - E_m^{(I)} \right) \mathbf{d}_{v,mn}^{ad,(I)} \quad (\text{G.9})$$

Using equation (10) in Carof, 17⁶⁸ and the Hellman-Feynman theorem we can rewrite equation (G.9) as equation (G.10):

$$\mathbf{F}_{eh,v}^{(I)} = \sum_{m,n} C_m^{*(I)} C_n^{(I)} \langle \psi_m | \nabla_v H | \psi_n \rangle \quad (\text{G.10})$$

We can substitute the coefficients and basis functions for those in equations (G.3) and (G.6). This carried out in equation (G.15). However, I have removed the trajectory and

atom index from the terms to make the notation clearer.

$$F_{eh,v} = \sum_{m,n} C_m^* C_n \langle \psi_m | \nabla H | \psi_n \rangle \quad (\text{G.11})$$

$$= \sum_{m,n} \sum_i u_i^* U_{im} \sum_j u_j U_{jn}^* \sum_l U_{lm}^* \sum_k U_{kn} \langle \phi_l | \nabla H | \phi_k \rangle \quad (\text{G.12})$$

$$= \sum_{m,n} \sum_{i,j,k,l} u_i^* u_j U_{im} U_{lm}^* U_{jn}^* U_{kn} \langle \phi_l | \nabla H | \phi_k \rangle \quad (\text{G.13})$$

$$= \sum_{i,j,k,l} u_i^* u_j \delta_{il} \delta_{jk} \langle \phi_l | \nabla H | \phi_k \rangle \quad (\text{G.14})$$

$$= \sum_{i,j} u_i^* u_j \langle \phi_i | \nabla H | \phi_j \rangle \quad (\text{G.15})$$

However, in the code the expectation value of the gradient of the Hamiltonian ($\langle \phi_i | \nabla H | \phi_j \rangle$) isn't very easily calculable. However, the gradient of the Hamiltonian matrix elements ($\nabla \langle \phi_i | H | \phi_j \rangle$) is easily calculable via the overlap term, $\nabla H = C \nabla S_{ij}$. Therefore, using chain rule we can re-write equation (G.15) as:

$$F_{eh,v} = \sum_{i,j} u_i^* u_j \langle \phi_i | \nabla H | \phi_j \rangle \quad (\text{G.16})$$

$$= \sum_{i,j} u_i^* u_j (\nabla \langle \phi_i | H | \phi_j \rangle - \langle \nabla \phi_i | H | \phi_j \rangle - \langle \phi_i | H | \nabla \phi_j \rangle) \quad (\text{G.17})$$

$$= \sum_{i,j} u_i^* u_j \left(\nabla \langle \phi_i | H | \phi_j \rangle - \sum_l \langle \nabla \phi_i | \phi_l \rangle \langle \phi_l | H | \phi_j \rangle - \sum_l \langle \phi_i | H | \phi_l \rangle \langle \phi_l | \nabla \phi_j \rangle \right) \quad (\text{G.18})$$

$$= \sum_{i,j} u_i^* u_j \left(\nabla \langle \phi_i | H | \phi_j \rangle + \sum_l \mathbf{d}_{il} \langle \phi_l | H | \phi_j \rangle - \sum_l \mathbf{d}_{lj} \langle \phi_i | H | \phi_l \rangle \right) \quad (\text{G.19})$$

Giving the final equation for the transformed forces as:

$$\mathbf{F}_{eh,v}^{(I)} = \sum_{i,j} \mathbf{u}_i^{*(I)} \mathbf{u}_j^{(I)} \left(\nabla_v H_{ij}^{(I)} + \sum_l \mathbf{d}_{lk,v}^{(I)} H_{lj}^{(I)} - \sum_l \mathbf{d}_{lj,v}^{(I)} H_{il} \right) \quad (\text{G.20})$$

Appendix H

Adiabatic State Initialisation

By diagonalising the Hamiltonian we get the adiabatic energies (eigenvalues) for each state and transformation matrix (eigenvectors) to calculate diabatic states \mathbb{U} . We can calculate diabatic coefficients corresponding to each adiabatic state via equation (H.1) below.

$$\mathbb{U}\mathbf{C}_n = \mathbf{u}_n \quad (\text{H.1})$$

Where \mathbb{U} is the transformation matrix of size $(N_{\text{mol}}, N_{\text{mol}})$, \mathbf{C} is a complex vector of size N_{mol} containing coefficients for adiabatic state n and \mathbf{u} is a complex vector of size N_{mol} containing coefficients for diabatic state n .

Seeing as we would like to find the diabatic population corresponding to each adiabatic state we localise coefficients on each pure adiabatic state and carry out the transformation e.g: $C_i = (1+0i, 0+0i, 0+0i, \dots)$ when we want to find the diabatic coefficient corresponding to state 1 and $C_i = (0+0i, 1+0i, 0+0i, \dots)$ when we want to find the diabatic coefficient corresponding to state 2 etc.. Therefore, the column, n , of the transformation matrix, \mathbb{U} , gives the diabatic coefficients corresponding to adiabatic state, n , as shown below in equation (H.2)

$$U_{in} = u_i \quad (\text{H.2})$$

Where n is the adiabatic state index and i is the diabatic (molecular) state index.

Once we have the diabatic state corresponding to each adiabatic state, and the en-

ergy of that adiabatic state, we can find which state best fulfills the requirements of being close to the center of the system and being within $3KT$ of the ground state. In order to do this, we can loop over each adiabatic state in increasing order of energy. The center of the system is calculated and the population weighted average center of mass, \mathbf{R}_n of the diabatic coefficients corresponding to adiabatic state n is calculated as in equation (H.3).

$$\mathbf{R}_n = \sum_i |u_i|^2 \mathbf{R}_{COM,i} \quad (\text{H.3})$$

The Euclidean distance between the center of the system and $\mathbf{R}_{COM,i}$ is calculated and if this distance is below some threshold value then we initialise the surface hopping trajectory on that adiabatic state. If we do not find any states within $3KT$ of the ground state and within an acceptable radius of the center we start again this time increasing the maximum allowed distance from the center. If this maximum allowed distance is increased such that we reach another threshold distance the energy threshold is increased this time until a state is found that is close enough to the center. In this way we find an adiabatic state, which when transformed, gives a diabatic population close to center of the system and near the ground state energy.

Appendix I

Center of Mass Restraints

The surface hopping code at the time did not support electrostatic interactions. So, in order to maintain the structure from the molecular dynamics simulations, center of mass restraints were used on each molecule.

The restraint set up for 1 molecule is shown in figure I.1. Here each of the 4 coloured zig-zag shapes show which atoms are restrained. These atoms were restrained about their center of mass. This configuration of restraints was used in order to stop rotations about the long axis for each molecule as this would allow molecules to form a face-to-face stacking giving rise to unphysically high couplings. The restraint strength was chosen to be the same as in another group members study to allow for a fair comparison of results. A short MD equilibration was performed to determine whether the restraint spring constant was sufficient to hold the molecules in place well enough to prevent the very high couplings appearing in the global coupling distribution. To further validate the choice of restraint/general set up a surface hopping simulation was carried out on a layer of bulk crystal and the mobilities were compared to known values.

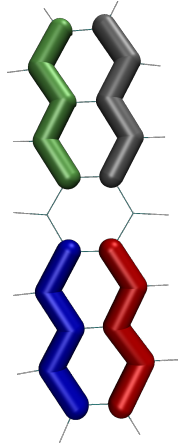


Figure I.1: The restraint set up for 1 molecule. Each coloured zig-zag shows the atoms that are restrained.

Appendix J

Active Systems

J.1 0ns and 1ns Systems

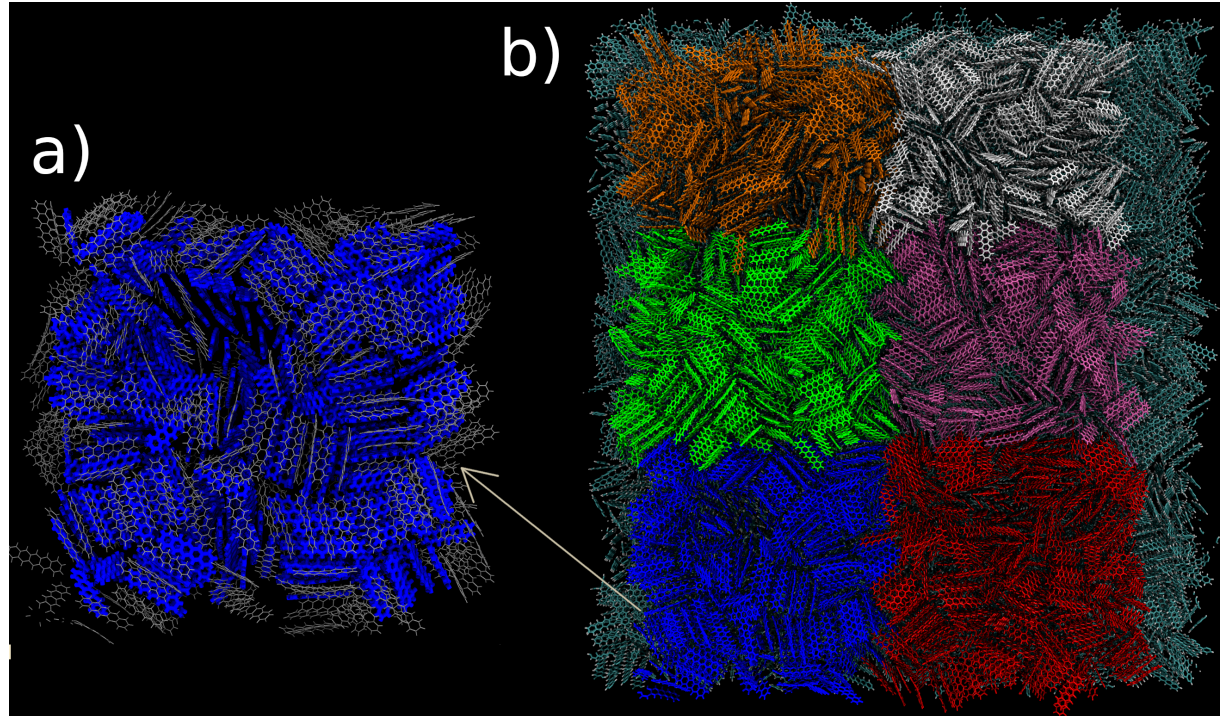


Figure J.1: Panel a) shows a system chosen to run surface hopping on, molecules in gray are fixed in place blue molecules show the active region. Panel b) shows every substructure chosen in the 0ns quenched structure.

The selection of the region for each surface hopping simulation was important in order to get a fair representation of the mobilities achievable within each structure. In the 0ns and 1ns quenched structures 6 slices were selected from the final snapshot of the structure. These were chosen to be independent clusters evenly spaced to sample

the mobility of the structure at various points. The selections are shown in figure J.1 for the 0ns quenched structure. The same process was used in the 1ns quenched structure.

In order to preserve the structure and maintain energy conservation a shell of inactive molecules was selected from the superstructure to surround the active region. The atoms within this remained fixed to their position at t=0.

J.2 100ns System

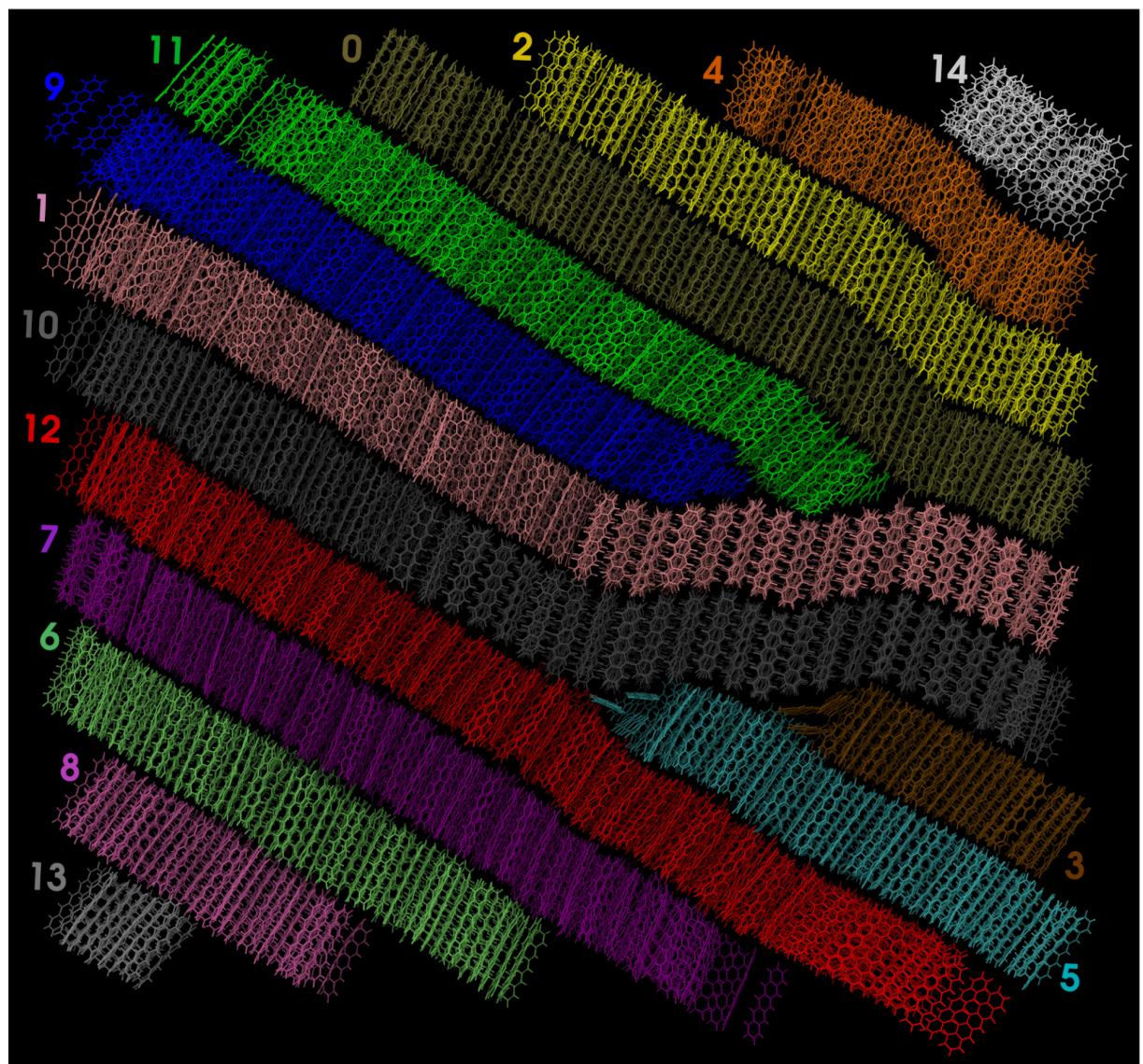


Figure J.2: The 100ns quenched structure clustered by layer. Each different colour represents a different cluster, labelled with the numbers around the edge of the structure.

The 100ns system is a much more ordered system and forms very well defined layers. This makes picking out structures on which to run surface hopping different to the 0/1ns quenched structures. The method I used was to first extend the superstructure in the z axis by $\pm 45\text{\AA}$ by repeating the periodic image and discarding molecules more than $\pm 45\text{\AA}$ from the simulation box boundaries. This was to ensure the resulting system was sufficiently large to converge mobilities. This added approximately 1 extra periodic image in the +ve and -ve z direction. A density based clustering algorithm (similar to DBSCAN¹¹³) was used to isolate the layers in the full structure by clustering centers of mass. These are shown in figure J.2. In this figure clusters 6, 7 and 11 were chosen to calculate the mobility via surface hopping.

J.3 10ns System

The choice of region within the 10ns quenched structure was different from the 0/1ns and the 100ns quenched structure. Here we have some large crystal fragments forming but still very few well defined layers. In this system the mobility is expected to be much more dependant on the initial position of the charge carrier within the structure than in the 0ns and 100ns quenched structure where the structure was more uniformly disordered or ordered respectively. In order to sample a reasonable range of mobilities in this structure 4 clusters were selected shown in fig J.3. 3 of these (red, blue and purple) were selected using a similar clustering procedure as in the 100ns quenched structure. The center-right green cluster was selected as it looked like it was a fairly disordered region where multiple crystal fragments

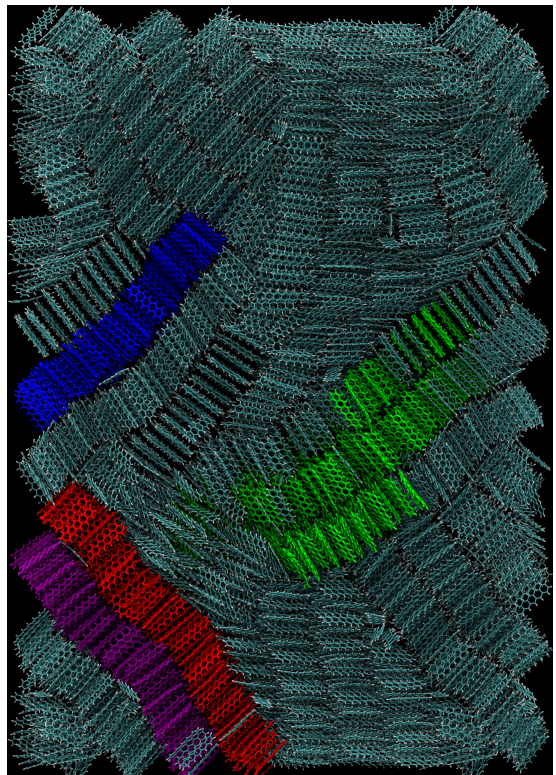


Figure J.3: The clusters chosen to run surface hopping simulations on. The coloured clusters each represent a different structure on which surface hopping was ran.

meet, which would give a lower bound on the mobility within the 10ns structure.

Appendix K

Additional Pentacene Mobility Information

Table K.1: Experimental and computed charge mobilities for amorphous, polycrystalline and single-crystalline pentacene.

Author	device/comp.	structure	gate dielectric	mobility	comm
1, Hesse80 2,	Photocurrent	amorphous		0.001-0.01 0.4	long t short
3, Bae13	TFT	amorphous	polymer	0.04-0.14	deper
4, Choo02	TFT	amorphous	SiN _x /p-Si	0.3	
5		amorphous-crystalline		0.1	
6, this work	comp.	amorphous		0.2	bulk,
7, Knipp04 8	TFT	polycrystalline	SiN ₃	0.2-0.55	grain
9, Fritz05 10	TFT	polycrystalline	thermal SiO ₂ +OTS	0.5-1.4	grain
11		polycrystalline	SiO ₂ rough	0.02	
12, Duffy08	TFT	polycrystalline	SiO ₂ smooth	0.31	large
13, Klauk02 14	TFT	polycrystalline	SiO ₂ +polymer	0.62	
15			SiO ₂ +BCB	0.4-0.7	
16, this work	comp.	nanocrystalline	SiO ₂	0.4	
17, this work	comp.	nanocrystalline	SiO ₂ +OTS	1.0	
18, this work	comp.	nanocrystalline	Si+polymer	3.0	
19, Zhang16 20, this work	OFET	2D single crystal	boronitride	0.2	bulk,
21, Zhang16	comp.	2D single crystal		0.9	bulk,
22, this work	OFET	2D single crystal	boronitride	1.8	bulk,
23, Lee06 24,	OFET	single crystal	SiO ₂	7.3	mono
25, Takeyama12	OFET	single crystal	Al ₂ O ₃ +ionic liquid	2.3	small
26, Arabi16	OFET	single crystal	SiO ₂	0.66	polym
27, this work	comp.	single crystal		5	crysta
				5.6	
				10.5	bulk,

Appendix L

Addition-Subtraction Forces

L.1 Real Space

The real space forces in the addition subtraction scheme are given in equation (L.1).

$$\mathbf{F}_i^\gamma = \begin{cases} \mathbf{F}_i^N(\mathbf{R}) + \sum_{j \in \gamma} (q_i^C q_j^C - q_i^N q_j^N) \mathbf{f}_{ij}(\mathbf{R}) + \sum_{j \notin \gamma} (q_i^C q_j^N - q_i^N q_j^N) \mathbf{f}_{ij}(\mathbf{R}); & i \in \gamma \\ \mathbf{F}_i^N(\mathbf{R}) - \sum_{j \in \gamma} (q_i^C q_j^N - q_i^N q_j^N) \mathbf{f}_{ij}(\mathbf{R}); & i \notin \gamma \end{cases} \quad (\text{L.1})$$

Where:

- $\mathbf{f}_{ij}(\mathbf{R}) = \frac{\hat{\mathbf{R}}_{ij}}{|\mathbf{R}_{ij}|} \left(\frac{\operatorname{erfc}(\alpha |\mathbf{R}_{ij}|)}{|\mathbf{R}_{ij}|} + \frac{2\alpha}{\sqrt{\pi}} e^{-\alpha^2 |\mathbf{R}_{ij}|^2} \right)$: the force between atoms i and j.
- $\mathbf{F}_i^N(\mathbf{R}) = q_i^N \sum_j^{N_{at}} q_j^N \mathbf{f}_{ij}(\mathbf{R})$: the total neutral force.
- q_j is the charge on atom j
- γ is the index of the charged molecule.

Once again, we first calculate the total force between all neutral molecules. The charge-charge interactions are substituted in for the neutral-neutral interactions for atoms on the charged molecule. The charge-neutral interactions are then substituted in for the neutral-neutral interactions for the charged molecule and its environment. The bonded interaction corrections are the same as these.

L.2 Reciprocal Space

The reciprocal space forces, as mentioned in the main text, cannot be decomposed with the addition-subtraction scheme.

$$\mathbf{F}_i^\gamma(\mathbf{R}) = \begin{cases} 4\pi q_i^C \sum_{\mathbf{k} \neq 0} \text{Im} [S'_\mathbf{k} E_{\mathbf{k},i}^*]; & i \in \gamma \\ 4\pi q_i^N \sum_{\mathbf{k} \neq 0} \text{Im} [S'_\mathbf{k} E_{\mathbf{k},i}^*]; & i \notin \gamma \end{cases} \quad (\text{L.2})$$

Where:

- $S'_\mathbf{k} = A_\mathbf{k} \left[\sum_j q_j^N E_{\mathbf{k},j} + \sum_{j \in \gamma} (q_j^C - q_j^N) E_{\mathbf{k},j} \right]$
- $A_\mathbf{k} = \frac{\mathbf{k}}{|\mathbf{k}|^2} e^{\frac{|\mathbf{k}|^2}{4\alpha^2}}$
- $E_{\mathbf{k},j} = e^{2\pi i \mathbf{k} \cdot \mathbf{R}_j}$

The calculation of this equation scales as $\mathcal{O}(N^3)$ where $N^3 = N_{\text{states}} N_{\text{at}} N_k$. This is because for every atom, i , in charged molecule, γ , a loop over \mathbf{k} vectors must be calculated.

Appendix M

Colophon

This document was set in the Times Roman typeface using L^AT_EX (specifically LuaTeX) and BibTeX+ make, composed with Vim.

Bibliography

- [1] Federica Agostini, Ali Abedi, Yasumitsu Suzuki, Seung Kyu Min, Neepa T. Maitra, and E. K. U. Gross. The exact forces on classical nuclei in non-adiabatic charge transfer. *The Journal of Chemical Physics*, 142(8):084303, February 2015.
- [2] Federica Agostini, Seung Kyu Min, Ali Abedi, and E. K. U. Gross. Quantum-Classical Nonadiabatic Dynamics: Coupled- vs Independent-Trajectory Methods. *Journal of Chemical Theory and Computation*, 12(5):2127–2143, May 2016.
- [3] Graeme H. Gossel, Federica Agostini, and Neepa T. Maitra. Coupled-Trajectory Mixed Quantum-Classical Algorithm: A Deconstruction. *Journal of Chemical Theory and Computation*, August 2018.
- [4] William Humphrey, Andrew Dalke, and Klaus Schulten. VMD – Visual Molecular Dynamics. *Journal of Molecular Graphics*, 14:33–38, 1996.
- [5] John Stone. An Efficient Library for Parallel Ray Tracing and Animation. Master’s thesis, Computer Science Department, University of Missouri-Rolla, April 1998.
- [6] C. K. Chiang, C. R. Fincher, Y. W. Park, A. J. Heeger, H. Shirakawa, E. J. Louis, S. C. Gau, and Alan G. MacDiarmid. Electrical Conductivity in Doped Polyacetylene. *Physical Review Letters*, 39(17):1098–1101, October 1977.
- [7] Hideki Shirakawa, Edwin J. Louis, Alan G. MacDiarmid, Chwan K. Chiang, and Alan J. Heeger. Synthesis of electrically conducting organic polymers: halogen derivatives of polyacetylene, $(CH)_x$. *J. Chem. Soc., Chem. Commun.*, 0(16):578–580, Jan 1977.

- [8] Bernard Kippelen and Jean-Luc Brédas. Organic photovoltaics. *Energy Environ. Sci.*, 2(3):251–261, 2009.
- [9] M. J. Małachowski and J. Żmija. Organic field-effect transistors. *Opto-Electron. Rev.*, 18(2):121–136, Jun 2010.
- [10] N. Thejo Kalyani and S. J. Dhoble. Organic light emitting diodes: Energy saving lighting technology—A review. *Renewable Sustainable Energy Rev.*, 16(5):2696–2723, Jun 2012.
- [11] Sebastian Reineke, Frank Lindner, Gregor Schwartz, Nico Seidler, Karsten Walzer, Björn Lüssem, and Karl Leo. White organic light-emitting diodes with fluorescent tube efficiency. *Nature*, 459(7244):234, May 2009.
- [12] Kazuki Kato, Toshihiko Iwasaki, and Takatoshi Tsujimura. Over 130 lm/w all-phosphorescent white oleds for next-generation lighting. *Journal of Photopolymer Science and Technology*, 28:335–340, 10 2015.
- [13] Veaceslav Coropceanu, Jérôme Cornil, Demetrio A. da Silva Filho, Yoann Olivier, Robert Silbey, and Jean-Luc Brédas. Charge Transport in Organic Semiconductors. *Chemical Reviews*, 107(4):926–952, April 2007.
- [14] Samuele Giannini, Antoine Carof, Matthew Ellis, Hui Yang, Orestis George Ziogos, Soumya Ghosh, and Jochen Blumberger. Quantum localization and delocalization of charge carriers in organic semiconducting crystals. *Nature Communications*, 10(1):3843, Aug 2019.
- [15] Alessandro Troisi. Charge transport in high mobility molecular semiconductors: classical models and new theories. *Chem. Soc. Rev.*, 40:2347–2358, 2011.
- [16] Simone Fratini, Didier Mayou, and Sergio Ciuchi. The transient localization scenario for charge transport in crystalline organic materials. *Advanced Functional Materials*, 26(14):2292–2315, 2016.

- [17] I. Yavuz. Dichotomy between the band and hopping transport in organic crystals: insights from experiments. *Physical Chemistry Chemical Physics*, 19(38):25819–25828, 2017.
- [18] Tahereh Nematiaran, Sergio Ciuchi, Xiaoyu Xie, Simone Fratini, and Alessandro Troisi. Practical computation of the charge mobility in molecular semiconductors using transient localization theory. *The Journal of Physical Chemistry C*, 123(12):6989–6997, Mar 2019.
- [19] S. Ciuchi, S. Fratini, and D. Mayou. Transient localization in crystalline organic semiconductors. *Phys. Rev. B*, 83:081202, Feb 2011.
- [20] Haobin Wang and Michael Thoss. A multilayer multiconfigurational time-dependent hartree study of vibrationally coupled electron transport using the scattering state representation. *The journal of physical chemistry. A*, 117, 03 2013.
- [21] Chr. Cattarius, G. A. Worth, H.-D. Meyer, and L. S. Cederbaum. All mode dynamics at the conical intersection of an octa-atomic molecule: Multi-configuration time-dependent Hartree (MCTDH) investigation on the butatriene cation. *The Journal of Chemical Physics*, 115(5):2088–2100, August 2001.
- [22] Uwe Manthe and Audrey Dell Hammerich. Wavepacket dynamics in five dimensions. photodissociation of methyl iodide. *Chemical Physics Letters*, 211(1):7–14, 1993.
- [23] U. Manthe, H.-D. Meyer, and L. S. Cederbaum. Multiconfigurational time-dependent hartree study of complex dynamics: Photodissociation of no₂. *The Journal of Chemical Physics*, 97(12):9062–9071, 1992.
- [24] A. Jäckle and H.-D. Meyer. Reactive scattering using the multiconfiguration time-dependent hartree approximation: General aspects and application to the collinear h+h₂→h₂+h reaction. *The Journal of Chemical Physics*, 102(14):5605–5615, 1995.
- [25] John C. Tully. Molecular dynamics with electronic transitions. *The Journal of Chemical Physics*, 93(2):1061–1071, 1990.

- [26] P. Ehrenfest. Bemerkung über die angenäherte gültigkeit der klassischen mechanik innerhalb der quantenmechanik. *Zeitschrift für Physik*, 45(7):455–457, Jul 1927.
- [27] D. F. Coker and L. Xiao. Methods for molecular dynamics with nonadiabatic transitions. *J. Chem. Phys.*, 102(1):496–510, Jan 1995.
- [28] Guangjun Nan, Xiaodi Yang, Linjun Wang, Zhigang Shuai, and Yi Zhao. Nuclear tunneling effects of charge transport in rubrene, tetracene, and pentacene. *Phys. Rev. B*, 79:115203, Mar 2009.
- [29] Sharon Hammes-Schiffer. Theoretical Perspectives on Proton-Coupled Electron Transfer Reactions. *Acc. Chem. Res.*, 34(4):273–281, Apr 2001.
- [30] Sharon Hammes-Schiffer and John C. Tully. Proton transfer in solution: Molecular dynamics with quantum transitions. *J. Chem. Phys.*, 101(6):4657–4667, Sep 1994.
- [31] My Hang V. Huynh and Thomas J. Meyer. Proton-coupled electron transfer. *Chemical Reviews*, 107(11):5004–5064, Nov 2007.
- [32] John C. Tully. Nonadiabatic Dynamics. pages 34–71.
- [33] Simone Pisana, Michele Lazzeri, Cinzia Casiraghi, Kostya S. Novoselov, A. K. Geim, Andrea C. Ferrari, and Francesco Mauri. Breakdown of the adiabatic Born–Oppenheimer approximation in graphene. *Nat. Mater.*, 6(3):198, Feb 2007.
- [34] M. Born and R. Oppenheimer. Zur Quantentheorie der Moleküle. *Ann. Phys.*, 389(20):457–484, Jan 1927.
- [35] Xiaosong Li, John C. Tully, H. Bernhard Schlegel, and Michael J. Frisch. Ab initio Ehrenfest dynamics. *J. Chem. Phys.*, 123(8):084106, Aug 2005.
- [36] Kenichiro Saita and Dmitrii V. Shalashilin. On-the-fly ab initio molecular dynamics with multiconfigurational Ehrenfest method. *J. Chem. Phys.*, 137(22):22A506, Dec 2012.
- [37] Daniela Kohen, Frank H. Stillinger, and John C. Tully. Model studies of nonadiabatic dynamics. *J. Chem. Phys.*, 109(12):4713–4725, Sep 1998.

- [38] John C. Tully. Perspective: Nonadiabatic dynamics theory. *The Journal of Chemical Physics*, 137(22):22A301, December 2012.
- [39] Priya V. Parandekar and John C. Tully. Detailed Balance in Ehrenfest Mixed Quantum-Classical Dynamics. *Journal of Chemical Theory and Computation*, 2(2):229–235, March 2006.
- [40] Samuele Giannini, Antoine Carof, and Jochen Blumberger. Crossover from hopping to band-like charge transport in an organic semiconductor model: Atomistic nonadiabatic molecular dynamics simulation. *The Journal of Physical Chemistry Letters*, 9(11):3116–3123, Jun 2018.
- [41] Antoine Carof, Samuele Giannini, and Jochen Blumberger. Detailed balance, internal consistency, and energy conservation in fragment orbital-based surface hopping. *The Journal of Chemical Physics*, 147(21):214113, 2017.
- [42] Linjun Wang, Alexey Akimov, and Oleg V. Prezhdo. Recent progress in surface hopping: 2011–2015. *The Journal of Physical Chemistry Letters*, 7(11):2100–2112, Jun 2016.
- [43] Linjun Wang and Oleg V. Prezhdo. A simple solution to the trivial crossing problem in surface hopping. *The Journal of Physical Chemistry Letters*, 5(4):713–719, Feb 2014.
- [44] Ali Abedi, Neepa T. Maitra, and E. K. U. Gross. Exact Factorization of the Time-Dependent Electron-Nuclear Wave Function. *Physical Review Letters*, 105(12), September 2010.
- [45] Federica Agostini, Seung Kyu Min, and E. K. U. Gross. Semiclassical analysis of the electron-nuclear coupling in electronic non-adiabatic processes. *Annalen der Physik*, 527(9-10):546–555, October 2015.
- [46] Federica Agostini, Ali Abedi, Yasumitsu Suzuki, and E.K.U. Gross. Mixed quantum-classical dynamics on the exact time-dependent potential energy surface: a fresh

- look at non-adiabatic processes. *Molecular Physics*, 111(22-23):3625–3640, December 2013.
- [47] Ali Abedi, Federica Agostini, Yasumitsu Suzuki, and E. K. U. Gross. Dynamical Steps that Bridge Piecewise Adiabatic Shapes in the Exact Time-Dependent Potential Energy Surface. *Physical Review Letters*, 110(26), June 2013.
- [48] Seung Kyu Min, Ali Abedi, Kwang S. Kim, and E. K. U. Gross. Is the Molecular Berry Phase an Artifact of the Born-Oppenheimer Approximation? *Phys. Rev. Lett.*, 113(26):263004, Dec 2014.
- [49] Todd J. Martínez*. Insights for Light-Driven Molecular Devices from Ab Initio Multiple Spawning Excited-State Dynamics of Organic and Biological Chromophores. American Chemical Society, Oct 2005.
- [50] Farnaz A. Shakib and Pengfei Huo. Ring Polymer Surface Hopping: Incorporating Nuclear Quantum Effects into Nonadiabatic Molecular Dynamics Simulations. *J. Phys. Chem. Lett.*, 8(13):3073–3080, Jul 2017.
- [51] Basile F. E. Curchod, Ivano Tavernelli, and Ursula Rothlisberger. Trajectory-based solution of the nonadiabatic quantum dynamics equations: an on-the-fly approach for molecular dynamics simulations. *PCCP*, 13(8):3231–3236, Feb 2011.
- [52] Ivano Tavernelli. Ab initio–driven trajectory-based nuclear quantum dynamics in phase space. *Phys. Rev. A*, 87(4):042501, Apr 2013.
- [53] Arne Scherrer, Federica Agostini, Daniel Sebastiani, E. K. U. Gross, and Rodolphe Vuilleumier. Nuclear velocity perturbation theory for vibrational circular dichroism: An approach based on the exact factorization of the electron-nuclear wave function. *J. Chem. Phys.*, 143(7):074106, Aug 2015.
- [54] Seung Kyu Min, Federica Agostini, Ivano Tavernelli, and E. K. U. Gross. Ab Initio Nonadiabatic Dynamics with Coupled Trajectories: A Rigorous Approach to Quantum (De)Coherence. *The Journal of Physical Chemistry Letters*, 8(13):3048–3055, July 2017.

- [55] John C. Tully. Molecular dynamics with electronic transitions. *The Journal of Chemical Physics*, 93(2):1061–1071, July 1990.
- [56] Fruzsina Gajdos, Siim Valner, Felix Hoffmann, Jacob Spencer, Marian Breuer, Adam Kubas, Michel Dupuis, and Jochen Blumberger. Ultrafast Estimation of Electronic Couplings for Electron Transfer between -Conjugated Organic Molecules. *Journal of Chemical Theory and Computation*, 10(10):4653–4660, October 2014.
- [57] J. VandeVondele, J; Hutter. Gaussian basis sets for accurate calculations on molecular systems in gas and condensed phases. *The Journal of Chemical Physics*, 127(11).
- [58] J. Spencer, F. Gajdos, and J. Blumberger. FOB-SH: Fragment orbital-based surface hopping for charge carrier transport in organic and biological molecules and materials. *The Journal of Chemical Physics*, 145(6):064102, August 2016.
- [59] Steven L. Fiedler and Jussi Eloranta. Nonadiabatic dynamics by mean-field and surface-hopping approaches: energy conservation considerations. *Molecular Physics*, 108(11):1471–1479, 2010.
- [60] Joseph E. Subotnik. Augmented ehrenfest dynamics yields a rate for surface hopping. *The Journal of Chemical Physics*, 132(13):134112, 2010.
- [61] K.E. Atkinson. An Introduction to Numerical Analysis. Wiley, 1989.
- [62] R.B. Leighton Richard P. Feynman. The Feynman Lectures on Physics, Vol 3. Addison–Wesley, 1998.
- [63] James Kirkpatrick. An approximate method for calculating transfer integrals based on the zindo hamiltonian. *International Journal of Quantum Chemistry*, 108(1):51–56, 2008.
- [64] Harald Oberhofer and Jochen Blumberger. Revisiting electronic couplings and incoherent hopping models for electron transport in crystalline c60 at ambient temperatures. *Phys. Chem. Chem. Phys.*, 14:13846–13852, 2012.

- [65] Alessandro Troisi and Giorgio Orlandi. Hole migration in dna: a theoretical analysis of the role of structural fluctuations. *The Journal of Physical Chemistry B*, 106(8):2093–2101, Feb 2002.
- [66] Adam Kubas, Felix Hoffmann, Alexander Heck, Harald Oberhofer, Marcus Elstner, and Jochen Blumberger. Electronic couplings for molecular charge transfer: Benchmarking cdft, fodft, and fodftb against high-level ab initio calculations. *The Journal of Chemical Physics*, 140(10):104105, 2014.
- [67] Adam Kubas, Fruzsina Gajdos, Alexander Heck, Harald Oberhofer, Marcus Elstner, and Jochen Blumberger. Electronic couplings for molecular charge transfer: benchmarking cdft, fodft and fodftb against high-level ab initio calculations. ii. *Phys. Chem. Chem. Phys.*, 17:14342–14354, 2015.
- [68] Antoine Carof, Samuele Giannini, and Jochen Blumberger. Detailed balance, internal consistency, and energy conservation in fragment orbital-based surface hopping. *The Journal of Chemical Physics*, 147(21):214113, December 2017.
- [69] Soumya Ghosh, Samuele Giannini, Kevin Lively, and Jochen Blumberger. Nonadiabatic dynamics with quantum nuclei: simulating charge transfer with ring polymer surface hopping. *Faraday Discuss.*, 221:501–525, 2020.
- [70] Antoine Carof, Samuele Giannini, and Jochen Blumberger. How to calculate charge mobility in molecular materials from surface hopping non-adiabatic molecular dynamics – beyond the hopping/band paradigm. *Phys. Chem. Chem. Phys.*, 21:26368–26386, 2019.
- [71] J. Spencer, F. Gajdos, and J. Blumberger. Fob-sh: Fragment orbital-based surface hopping for charge carrier transport in organic and biological molecules and materials. *The Journal of Chemical Physics*, 145(6):064102, 2016.
- [72] Jacob Spencer, Laura Scalfi, Antoine Carof, and Jochen Blumberger. Confronting surface hopping molecular dynamics with marcus theory for a molecular donor–acceptor system. *Faraday Discuss.*, 195:215–236, 2016.

- [73] Samuele Giannini, Orestis George Ziogos, Antoine Carof, Matthew Ellis, and Jochen Blumberger. Flickering polarons extending over ten nanometres mediate charge transport in high-mobility organic crystals. *Advanced Theory and Simulations*, 3(9):2000093, 2020.
- [74] Orestis George Ziogos, Samuele Giannini, Matthew Ellis, and Jochen Blumberger. Identifying high-mobility tetracene derivatives using a non-adiabatic molecular dynamics approach. *J. Mater. Chem. C*, 8:1054–1064, 2020.
- [75] Fruzsina Gajdos, Siim Valner, Felix Hoffmann, Jacob Spencer, Marian Breuer, Adam Kubas, Michel Dupuis, and Jochen Blumberger. Ultrafast estimation of electronic couplings for electron transfer between π -conjugated organic molecules. *Journal of Chemical Theory and Computation*, 10(10):4653–4660, Oct 2014.
- [76] Biswajit Ray, Aditya G. Baradwaj, Bryan W. Boudouris, and Muhammad A. Alam. Defect characterization in organic semiconductors by forward bias capacitance–voltage (fb-cv) analysis. *The Journal of Physical Chemistry C*, 118(31):17461–17466, Aug 2014.
- [77] W. S. Hu, Y. T. Tao, Y. J. Hsu, D. H. Wei, and Y. S. Wu. Molecular orientation of evaporated pentacene films on gold: alignment effect of self-assembled monolayer. *Langmuir*, 21(6):2260–2266, Mar 2005.
- [78] Tatsuo Hasegawa and Jun Takeya. Organic field-effect transistors using single crystals. *Science and Technology of Advanced Materials*, 10(2):024314, 2009.
- [79] John E. Anthony, James S. Brooks, David L. Eaton, and Sean R. Parkin. Functionalized pentacene: improved electronic properties from control of solid-state order. *Journal of the American Chemical Society*, 123(38):9482–9483, Sep 2001.
- [80] John E. Anthony, David L. Eaton, and Sean R. Parkin. A road map to stable, soluble, easily crystallized pentacene derivatives. *Organic Letters*, 4(1):15–18, Jan 2002.

- [81] A. D'Angelo, B. Edgar, A. P. Hurt, and M. D. Antonijević. Physico-chemical characterisation of three-component co-amorphous systems generated by a melt-quench method. *Journal of Thermal Analysis and Calorimetry*, 134(1):381–390, Oct 2018.
- [82] Wanderlã L. Scopel, Antônio J. R. da Silva, and A. Fazzio. Amorphous hfo_2 and $\text{hf}_{1-x}\text{si}_x\text{O}$ via a melt-and-quench scheme using ab initio molecular dynamics. *Phys. Rev. B*, 77:172101, May 2008.
- [83] Seth S. Berbano, Inseok Seo, Christian M. Bischoff, Katherine E. Schuller, and Steve W. Martin. Formation and structure of $\text{na}_2\text{s}+\text{p}_2\text{s}_5$ amorphous materials prepared by melt-quenching and mechanical milling. *Journal of Non-Crystalline Solids*, 358(1):93 – 98, 2012.
- [84] Pranav Karmwar, Kirsten Graeser, Keith C. Gordon, Clare J. Strachan, and Thomas Rades. Investigation of properties and recrystallisation behaviour of amorphous indomethacin samples prepared by different methods. *International Journal of Pharmaceutics*, 417(1):94 – 100, 2011. Advanced characterization techniques.
- [85] Min-Jin Ko, Joel Plawsky, and Meyer Birnboim. Fabrication of cds/ag hybrid quantum dot composites using a melt/quench method. *Journal of Non-Crystalline Solids*, 203:211 – 216, 1996. Optical and Electrical Propertias of Glasses.
- [86] Steve Plimpton. Fast parallel algorithms for short-range molecular dynamics. *Journal of Computational Physics*, 117(1):1 – 19, 1995.
- [87] Steve Plimpton. Lammps software. <http://lammps.sandia.gov>, 1995. [Online; accessed 21-Jan-2021].
- [88] Steve Plimpton, Roy Pollock, and Mark Stevens. Particle-mesh ewald and rRESPA for parallel molecular dynamics simulations. In In Proceedings of the Eighth SIAM Conference on Parallel Processing for Scientific Computing, 1997.
- [89] Christopher I. Bayly, Piotr Cieplak, C, and Peter A. Kollman. A well-behaved electrostatic potential based method using charge restraints for deriving atomic

- charges: the resp model. *The Journal of Physical Chemistry*, 97(40):10269–10280, Oct 1993.
- [90] M. J. Frisch, G. W. Trucks, H. B. Schlegel, G. E. Scuseria, M. A. Robb, J. R. Cheeseman, G. Scalmani, V. Barone, G. A. Petersson, H. Nakatsuji, X. Li, M. Caricato, A. V. Marenich, J. Bloino, B. G. Janesko, R. Gomperts, B. Mennucci, H. P. Hratchian, J. V. Ortiz, A. F. Izmaylov, J. L. Sonnenberg, D. Williams-Young, F. Ding, F. Lipparini, F. Egidi, J. Goings, B. Peng, A. Petrone, T. Henderson, D. Ranasinghe, V. G. Zakrzewski, J. Gao, N. Rega, G. Zheng, W. Liang, M. Hada, M. Ehara, K. Toyota, R. Fukuda, J. Hasegawa, M. Ishida, T. Nakajima, Y. Honda, O. Kitao, H. Nakai, T. Vreven, K. Throssell, J. A. Montgomery, Jr., J. E. Peralta, F. Ogliaro, M. J. Bearpark, J. J. Heyd, E. N. Brothers, K. N. Kudin, V. N. Staroverov, T. A. Keith, R. Kobayashi, J. Normand, K. Raghavachari, A. P. Rendell, J. C. Burant, S. S. Iyengar, J. Tomasi, M. Cossi, J. M. Millam, M. Klene, C. Adamo, R. Cammi, J. W. Ochterski, R. L. Martin, K. Morokuma, O. Farkas, J. B. Foresman, and D. J. Fox. Gaussian~16 Revision C.01, 2016. Gaussian Inc. Wallingford CT.
- [91] Junmei Wang, Romain M. Wolf, James W. Caldwell, Peter A. Kollman, and David A. Case. Development and testing of a general amber force field. *Journal of Computational Chemistry*, 25(9):1157–1174, 2004.
- [92] Makoto Yoneya, Masahiro Kawasaki, and Masahiko Ando. Molecular dynamics simulations of pentacene thin films: The effect of surface on polymorph selection. *J. Mater. Chem.*, 20:10397–10402, 2010.
- [93] Makoto Yoneya, Masahiro Kawasaki, and Masahiko Ando. Are pentacene monolayer and thin-film polymorphs really substrate-induced? a molecular dynamics simulation study. *The Journal of Physical Chemistry C*, 116(1):791–795, Jan 2012.
- [94] Makoto Yoneya. Simulation of crystallization of pentacene and its derivatives from solution. *The Journal of Physical Chemistry C*, Jan 2021.

- [95] Ryan A. Miller, Amanda Larson, and Karsten Pohl. Novel surface diffusion characteristics for a robust pentacene derivative on au(111) surfaces. *Chemical Physics Letters*, 678:28 – 34, 2017.
- [96] Dong Wang, Ling Tang, Mengqiu Long, and Zhigang Shuai. Anisotropic thermal transport in organic molecular crystals from nonequilibrium molecular dynamics simulations. *The Journal of Physical Chemistry C*, 115(13):5940–5946, Apr 2011.
- [97] Florian Steiner, Carl Poelking, Dorota Niedzialek, Denis Andrienko, and Jenny Nelson. Influence of orientation mismatch on charge transport across grain boundaries in tri-isopropylsilyl lethynyl (tips) pentacene thin films. *Phys. Chem. Chem. Phys.*, 19:10854–10862, 2017.
- [98] Ida Bagus Hendra Prastiawan, Jingxiang Xu, Yusuke Ootani, Yuji Higuchi, Nobuki Ozawa, Shingo Maruyama, Yuji Matsumoto, and Momoji Kubo. Molecular interactions between pentacene and imidazolium ionic liquids: A molecular dynamics study. *Chemistry Letters*, 47(9):1154–1157, 2018.
- [99] EPA DSSTox. Epa dsstox. <https://comptox.epa.gov/dashboard/DTXSID7059648>, 2021. [Online; accessed 25-Jan-2021].
- [100] Stefan Schiefer, Martin Huth, Alexander Dobrinevski, and Bert Nickel. Determination of the crystal structure of substrate-induced pentacene polymorphs in fiber structured thin films. *Journal of the American Chemical Society*, 129(34):10316–10317, Aug 2007.
- [101] R. B. Campbell, J. M. Robertson, and J. Trotter. The crystal and molecular structure of pentacene. *Acta Crystallographica*, 14(7):705–711, Jul 1961.
- [102] Yoko Takeyama, Shimpei Ono, and Yuji Matsumoto. Organic single crystal transistor characteristics of single-crystal phase pentacene grown by ionic liquid-assisted vacuum deposition. *Applied Physics Letters*, 101(8):083303, 2012.
- [103] S. Atika Arabi, Ji Dong, Misbah Mirza, Peng Yu, Liang Wang, Jun He, and Chao

- Jiang. Nanoseed assisted pvt growth of ultrathin 2d pentacene molecular crystal directly onto sio2 substrate. *Crystal Growth & Design*, 16(5):2624–2630, May 2016.
- [104] Yuhang Zhang, Jingsi Qiao, Si Gao, Fengrui Hu, Daowei He, Bing Wu, Ziyi Yang, Bingchen Xu, Yun Li, Yi Shi, Wei Ji, Peng Wang, Xiaoyong Wang, Min Xiao, Hangxun Xu, Jian-Bin Xu, and Xinran Wang. Probing carrier transport and structure–property relationship of highly ordered organic semiconductors at the two-dimensional limit. *Phys. Rev. Lett.*, 116:016602, Jan 2016.
- [105] Thorsten Vehoff, Yeon Sook Chung, Karen Johnston, Alessandro Troisi, Do Y. Yoon, and Denis Andrienko. Charge transport in self-assembled semiconducting organic layers: Role of dynamic and static disorder. *The Journal of Physical Chemistry C*, 114(23):10592–10597, Jun 2010.
- [106] Wei-Qiao Deng and William A. Goddard. Predictions of hole mobilities in oligoacene organic semiconductors from quantum mechanical calculations. *The Journal of Physical Chemistry B*, 108(25):8614–8621, Jun 2004.
- [107] Joe J. Kwiatkowski, Jarvist M. Frost, and Jenny Nelson. The effect of morphology on electron field-effect mobility in disordered c₆₀ thin films. *Nano Letters*, 9(3):1085–1090, Mar 2009.
- [108] Stavros Athanasopoulos, James Kirkpatrick, Diego Martínez, Jarvist M. Frost, Clare M. Foden, Alison B. Walker, and Jenny Nelson. Predictive study of charge transport in disordered semiconducting polymers. *Nano Letters*, 7(6):1785–1788, Jun 2007.
- [109] Thorsten Vehoff, Björn Baumeier, Alessandro Troisi, and Denis Andrienko. Charge transport in organic crystals: Role of disorder and topological connectivity. *Journal of the American Chemical Society*, 132(33):11702–11708, Aug 2010.
- [110] Pascal Kordt and Denis Andrienko. Modeling of spatially correlated energetic disorder in organic semiconductors. *Journal of Chemical Theory and Computation*, 12(1):36–40, Jan 2016.

- [111] Yuan Zhang, Ling-Kun Meng, Jin Hu, Rui-Ke Zou, Chao Tang, Gong Li, Yan Ding, Hai-Tong Cai, Zhi-Yao Yang, and Wei Huang. Theoretical exploration of carrier dynamics in amorphous pyrene–fluorene derivative organic semiconductors. *ACS Omega*, 4(9):14124–14132, Aug 2019.
- [112] Orestis George Ziogos, Samuele Giannini, Matthew Ellis, and Jochen Blumberger. Identifying high-mobility tetracene derivatives using a non-adiabatic molecular dynamics approach. *J. Mater. Chem. C*, 8:1054–1064, 2020.
- [113] Martin Ester, Hans-Peter Kriegel, Jörg Sander, and Xiaowei Xu. A density-based algorithm for discovering clusters in large spatial databases with noise. pages 226–231. AAAI Press, 1996.
- [114] R. Hesse and H. Bässler. Short-time carrier transport in amorphous pentacene. *physica status solidi (b)*, 101(2):481–487, 1980.
- [115] Jin-Hyuk Bae, Sin-Doo Lee, and Chang-Jae Yu. Deposition rate dependent mobility of an organic transistor with an anisotropic polymeric insulator. *Solid-State Electronics*, 79:98–103, 2013.
- [116] M. H. Choo, Jae Hoon Kim, and Seongil Im. Hole transport in amorphous-crystalline-mixed and amorphous pentacene thin-film transistors. *Applied Physics Letters*, 81(24):4640–4642, 2002.
- [117] D. Knipp and R.A. Street. Pentacene thin film transistors on large area compatible gate dielectrics. *Journal of Non-Crystalline Solids*, 338-340:595–598, 2004. Proceedings of the 20th International Conference on Amorphous and Microcrystalline Semiconductors.
- [118] Nicolas G. Martinelli, Matteo Savini, Luca Muccioli, Yoann Olivier, Frédéric Castet, Claudio Zannoni, David Beljonne, and Jérôme Cornil. Modeling polymer dielectric/pentacene interfaces: On the role of electrostatic energy disorder on charge carrier mobility. *Advanced Functional Materials*, 19(20):3254–3261, 2009.

- [119] P. P. Ewald. Die berechnung optischer und elektrostatischer gitterpotentiale. *Annalen der Physik*, 369(3):253–287, 1921.
- [120] Abdulnour Y. Toukmaji and John A. Board. Ewald summation techniques in perspective: a survey. *Computer Physics Communications*, 95(2):73–92, 1996.
- [121] D. Wolf, P. Kebinski, S. R. Phillpot, and J. Eggebrecht. Exact method for the simulation of coulombic systems by spherically truncated, pairwise $r-1$ summation. *The Journal of Chemical Physics*, 110(17):8254–8282, 1999.
- [122] Dirk Zahn, Bernd Schilling, and Stefan M. Kast. Enhancement of the wolf damped coulomb potential: static, dynamic, and dielectric properties of liquid water from molecular simulation. *The Journal of Physical Chemistry B*, 106(41):10725–10732, Oct 2002.
- [123] Christopher J. Fennell and J. Daniel Gezelter. Is the ewald summation still necessary? pairwise alternatives to the accepted standard for long-range electrostatics. *The Journal of Chemical Physics*, 124(23):234104, 2006.
- [124] Colin R. Groom, Ian J. Bruno, Matthew P. Lightfoot, and Suzanna C. Ward. The Cambridge Structural Database. *Acta Crystallographica Section B*, 72(2):171–179, Apr 2016.
- [125] Pavlo O. Dral, Mario Barbatti, and Walter Thiel. Nonadiabatic excited-state dynamics with machine learning. *The Journal of Physical Chemistry Letters*, 9(19):5660–5663, Oct 2018.